JCB Journal of Cell Biology

ARTICLE

Convergence of secretory, endosomal, and autophagic routes in trans-Golgi–associated lysosomes

Lingjian Zhou[1*], Xutong Xue[1*], Ke Yang[1], Zhi Feng[1], Min Liu[1], and José C. Pastor-Pareja[1,2,3]

At the trans-Golgi, complex traffic connections exist to the endolysosomal system additional to the main Golgi-to–plasma membrane secretory route. Here, we investigated three hits in a *Drosophila* screen displaying secretory cargo accumulation in autophagic vesicles: ESCRT-III component Vps20, SNARE-binding Rop, and lysosomal pump subunit VhaPPA1-1. We found that Vps20, Rop, and lysosomal markers localize near the trans-Golgi. Furthermore, we document that the vicinity of the trans-Golgi is the main cellular location for lysosomes and that early, late, and recycling endosomes associate as well with a trans-Golgi–associated degradative compartment where basal microautophagy of secretory cargo and other materials occurs. Disruption of this compartment causes cargo accumulation in our hits, including Munc18 homolog Rop, required with Syx1 and Syx4 for Rab11-mediated endosomal recycling. Finally, besides basal microautophagy, we show that the trans-Golgi–associated degradative compartment contributes to the growth of autophagic vesicles in developmental and starvation-induced macroautophagy. Our results argue that the fly trans-Golgi is the gravitational center of the whole endomembrane system.

Introduction

In the early secretory pathway, cargoes are collected at specialized regions of the ER called ER exit sites (ERES) preceding transport to the Golgi apparatus (Bannykh et al., 1996). The Golgi apparatus is a polarized stack of cisternae divided into cis-, mid-, and trans-Golgi regions based on the presence of different proteins (Klumperman, 2011). Thanks in large part to genetic screening, we know many factors involved in the exit of secretory cargoes from ERES and their arrival to the cis-Golgi (Bard et al., 2006; Novick et al., 1980; Wendler et al., 2010). As a result, molecular events taking place at the ER–Golgi interface are relatively well understood (Barlowe and Miller, 2013; Brandizzi and Barlowe, 2013). Much less is known, however, about the organization and function of the trans-Golgi. The trans-most cisterna of the Golgi and associated membranes of the TGN function as a sorting station for the transport of cargoes to the plasma membrane, but also to other subcellular locations (De Matteis and Luini, 2008; Klumperman and Raposo, 2014). Indeed, ample evidence shows complex traffic connections between the trans-Golgi and the endolysosomal system (Braulke and Bonifacino, 2009; van Meel and Klumperman, 2008), in contrast to the tightly canalized nature of exchanges between the ER and cis-Golgi. Consequently, organization of the trans-Golgi and connections between the trans-Golgi and the endolysosomal system is poorly understood.

At the end of the endolysosomal system lie lysosomes: degradative organelles increasingly recognized as major cellular signaling centers (Jouandin et al., 2022; Lim and Zoncu, 2016). Inside lysosomes, catabolic processes take place in a highly acidic environment maintained by pumping of protons through the vacuolar H^+ ATPase pump (v-ATPase; Xu and Ren, 2015). In the endolysosomal system, additionally comprising early, late, and recycling endosomal compartments, cargo destined to be degraded arrives at lysosomes from the cell surface (Klumperman and Raposo, 2014). Endocytosis of extracellular or cell surface cargo begins with the internalization and fission of plasma membrane to form endocytic vesicles, which undergo a series of maturation steps to become early and late endosomes (Huotari and Helenius, 2011). In late endosomes, cargoes destined for degradation are sorted into intraluminal vesicles by the action of the ESCRT (endosomal sorting complexes required for transport) machinery to form multivesicular bodies (Vietri et al., 2020), which then fuse with lysosomes with the assistance of

[1]School of Life Sciences, Tsinghua University, Beijing, China; [2]Tsinghua-Peking Center for Life Sciences, Beijing, China; [3]Institute of Neurosciences, Consejo Superior de Investigaciones Científicas–Universidad Miguel Hernández, San Juan de Alicante, Spain.

*L. Zhou and X. Xue contributed equally to this paper. Correspondence to José C. Pastor-Pareja: jose.pastorp@umh.es.

SNARE proteins (Luzio et al., 2014). In a homeostatic process parallel to the endolysosomal pathway, cellular materials such as protein aggregates and whole organelles are delivered to lysosomes through autophagy (Galluzzi et al., 2017). Two main autophagic routes exist, depending on how cellular materials reach the lysosome. In the first one, microautophagy, lysosomes, or late endosomes directly engulf small portions of cytoplasm. Although microautophagy was observed early after the discovery of lysosomes, mechanistic details are still scarce (Yim and Mizushima, 2020). In macroautophagy, the second, best-studied route, portions of cytoplasm including whole organelles are captured by a membrane cisterna that closes on itself to produce double membrane autophagosomes, which then fuse with lysosomes and give rise to autophagic vesicles (autolysosomes). Besides the well-established roles of endosomal pathways in autophagy (Tooze et al., 2014), there is support as well for a strong connection between macroautophagy and secretion (Wang et al., 2017). Work by many groups in the last decade has focused on contributions from ERES and the vertebrate ER–Golgi intermediate compartment to the growth of autophagic vesicles (Cui et al., 2019; Farhan et al., 2017; Ge et al., 2013; Graef et al., 2013; Omari et al., 2018; Rabouille, 2019; Wang et al., 2013; Zoppino et al., 2010). However, multiple other pieces of evidence (De Tito et al., 2020; Deng et al., 2020; Ohashi and Munro, 2010; Young et al., 2006) link secretory pathway membranes to macroautophagy at the level of the Golgi and TGN instead.

The fruit fly *Drosophila* is an excellent system for studying secretion in an animal. Most proteins known to play roles in secretion are conserved in flies (Kondylis and Rabouille, 2009). In *Drosophila*, contrary to vertebrates, but same as the rest of animals, plants, and unicellular eukaryotes, multiple Golgi stacks are distributed throughout the cytoplasm in close proximity to ERES forming independent ERES-Golgi units (Feng et al., 2020; Kondylis and Rabouille, 2009; Ripoche et al., 1994). *Drosophila* is also a superb system to study autophagy induction signals and the cascades mediating autophagic vesicle formation (Maruzs et al., 2019; Mauvezin et al., 2014; Mulakkal et al., 2014; Zhang and Baehrecke, 2015; Rahman et al., 2022). Research in *Drosophila* has produced in vivo evidence and biological insights into the roles of autophagy in normal development (Lee and Baehrecke, 2001), cancer (Bilder et al., 2021; Katheder et al., 2017) and into less understood areas such as basal autophagy (Simonsen et al., 2008) and microautophagy triggered by starvation or other cellular stresses (Jacomin et al., 2021; Mesquita et al., 2021; Mukherjee et al., 2016). Many of these studies have taken advantage of the larval fat body as a convenient experimental model. The fat body, equivalent to human adipose tissue and liver, undergoes developmentally programmed autophagy during the wandering stage of the third larval instar (L3), prior to metamorphosis (Rusten et al., 2004). In addition, upon nutrient deprivation, the fat body quickly undergoes starvation-induced autophagy (Scott et al., 2004). Besides lipid storage and metabolic roles, the fat body is a highly secretory tissue producing most Collagen IV and other extracellular matrix of the animal (Pastor-Pareja, 2020; Pastor-Pareja and Xu, 2011; Fig. 1 A). Lysosome biogenesis in the fat body requires endosomal traffic (Jacomin et al., 2016), but a relation between degradative and secretory traffic has not been explored. For studying relations among secretion, the endolysosomal system and autophagy, *Drosophila* provides a very distinct advantage in the form of limited gene redundancy, sophisticated genetic tools and the possibility of conducting unbiased genetic screening.

Here, we studied three hits in a secretion screening we previously conducted (Ke et al., 2018). In these hits, namely a SNARE-binding protein, an ESCRT-III complex member, and a component of the v-ATPase proton pump, we found that Collagen IV accumulated inside autophagic vesicles. When we further characterized these hits, we found that failure of a basal autophagic process taking place in lysosomes located in the vicinity of the trans-Golgi (trans-Golgi–associated lysosomes) was responsible for cargo accumulation. Moreover, we found that, beyond lysosomes, the trans-Golgi is the major location for the whole endolysosomal system in *Drosophila* cells, which supports rethinking of the trans-Golgi/TGN as a true endocytic-secretory hybrid organelle in this animal.

Results

Secretion screening hits *Rop*, *Vps20*, and *VhaPPA1-1* retain cargo inside autophagic vesicles in fat body adipocytes

In an RNAi screen for genes involved in collagen secretion by fat body adipocytes, we previously found 88 hits producing intracellular retention of basement membrane Collagen IV (Ke et al., 2018). While a majority of hits displayed accumulation of Collagen IV (Vkg-GFP) in bags of dilated ER caused by defective ER-to-Golgi transport (Fig. S1 A), three hits displayed unusual collagen distribution. These were the Munc18 ortholog Rop (Ras opposite), ESCRT component Vps20 (vacuolar protein sorting 20), and the VhaPPA1-1 subunit of the v-ATPase proton pump. In these hits (Fig. 1 B; confirmation with alternative RNAi transgenes in Fig. S1, A and B), retained collagen was found inside membrane vesicles labeled by myr-RFP (myristoylation domain of Src fused to RFP). This defect was not specific to Collagen IV, since the general secretion marker secr-GFP (Pfeiffer et al., 2002) also accumulated in myr-RFP–positive vesicles (Fig. 1 C). Upon closer examination, myr-RFP–positive vesicles containing Collagen IV or secr-GFP seemed to contain other vesicles inside, reminiscent of autophagic vesicles, also due to their large size. To test whether these were indeed autophagic vesicles, we examined autophagy marker Atg8a-mCherry after Vps20, Rop, and VhaPPA1-1 knockdown and found that collagen accumulated inside Atg8a-positive vesicles (Fig. 1 D). Furthermore, using the thermosensitive GAL4 repressor GAL80^{ts} for temporal control of GAL4-induced RNAi (McGuire et al., 2003; see Materials and methods), we found that in all three hits Atg8 and Collagen IV puncta were initially separate (Fig. S1 C). Consistent also with an autophagic nature for these vesicles, imaging through transmission electron microscopy (TEM) revealed that they contained smaller vesicles inside, as well as dense material and darkened condensates (Fig. 1 E). LysoTracker staining, finally, revealed reduced acidification of the vesicles formed upon Rop, Vps20, and VhaPPA1-1 knockdown (Fig. S1, D–F), suggesting defects in autophagic degradation. Altogether, these results show that

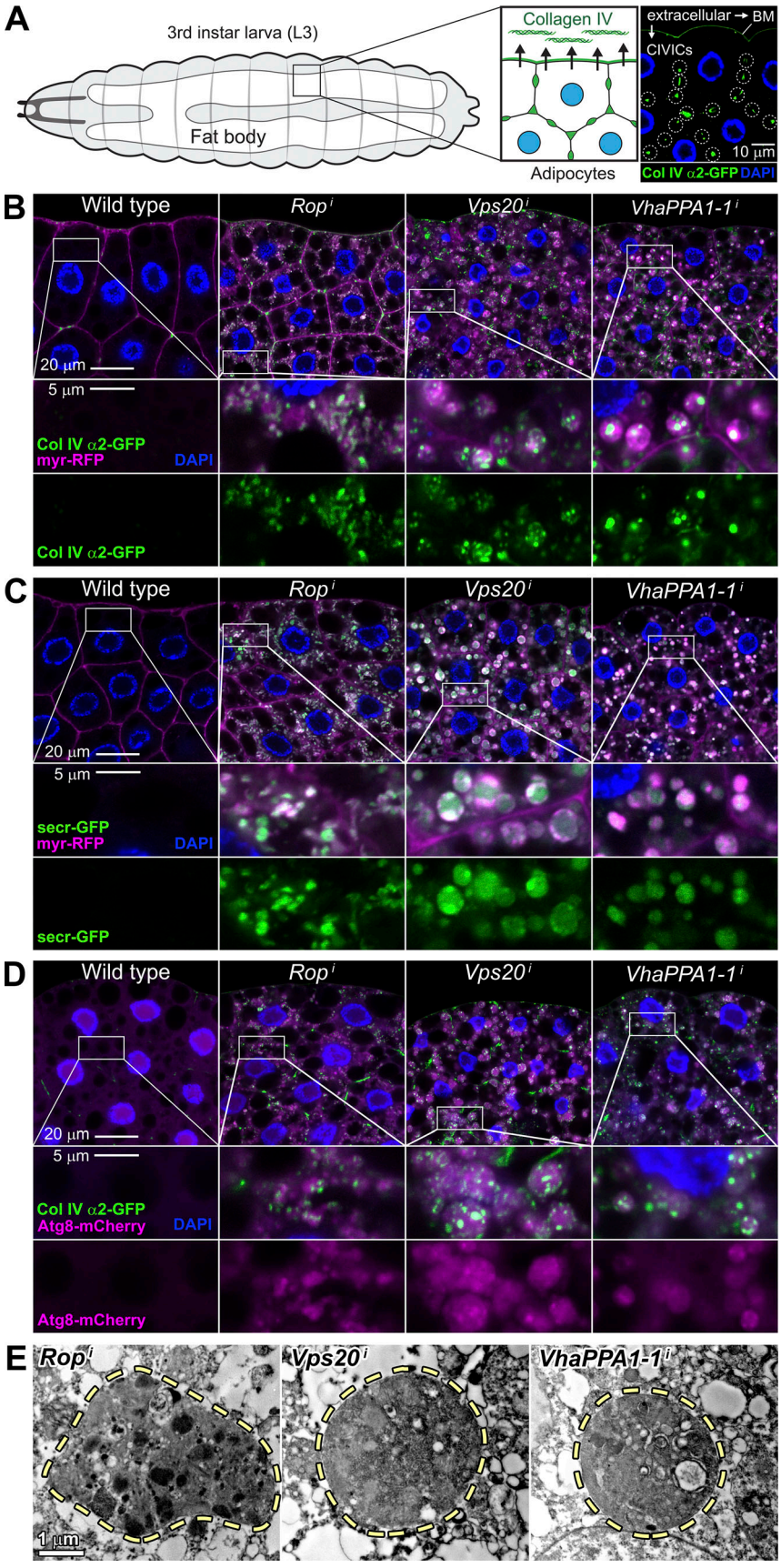

Figure 1. **Secretion screening hits *Rop*, *vps20*, and *VhaPPA1-1* retain cargo inside autophagic vesicles in fat body adipocytes. (A)** Schematic drawing of the *Drosophila* fat body next to a confocal image of L3 adipocytes (feeding stage). In the wild type, Collagen IV is only seen in the basement membrane (BM) that surrounds the tissue and in the equally extracellular CIVICs (Collagen IV intercellular concentrations, circled; Dai et al., 2017). Collagen IV in green (α2 chain Vkg-GFP) and nuclei in blue (DAPI staining). **(B)** Confocal images of L3 fat body (feeding stage) from wild-type, *BM-40-SPARC>Rop^i* (v19696), *>Vps20^i* (THU5269), and *>VhaPPA1-1^i* (TH04233.N) larvae, showing localization of Collagen IV (α2 chain Vkg-GFP, green). Plasma membrane labeled with *BM-40-SPARC-GAL4*-driven myr-RFP (magenta). DAPI in blue. Magnified images show accumulation of Collagen IV in large myr-RFP–positive vesicles in mutant conditions. **(C)** Fat body from wild-type, *BM-40-SPARC>Rop^i*, *>Vps20^i*, and *>VhaPPA1-1^i* L3 larvae showing localization of *BM-40-SPARC-GAL4*–driven general secretion marker secr-GFP (Wg signal peptide fused to GFP, green). Magnified images show accumulation of secr-GFP in myr-RFP–positive (magenta) vesicles in mutant conditions. **(D)** Fat body from wild-type, *BM-40-SPARC>Rop^i*, *>Vps20^i*, and *>VhaPPA1-1^i* L3 larvae showing localization of Collagen IV (Vkg-GFP, green) and *BM-40-SPARC-GAL4*–driven autophagy marker Atg8a-mCherry (magenta). Magnified insets show accumulation of Collagen IV in Atg8a-positive vesicles in mutant conditions. **(E)** TEM images of autophagic vesicles (defective autolysosomes, inside dashed lines) from L3 fat body (feeding stage) in *BM-40-SPARC>Rop^i* (v19696), *>Vps20^i* (THU5269), and *>VhaPPA1-1^i* (v47188) larvae.

knockdown of Rop, Vps20, and VhaPPA1-1 causes defective accumulation of secretory cargoes in autophagic vesicles.

Localization of Rop, Vps20, lysosomal markers, and endosomal Rab-GTPases near Golgi

Intrigued by the link between secretory and degradative pathways hinted by these hits, we investigated them further. We first created GFP-tagged versions of Rop and Vps20, expressed them under control of the GAL4/UAS system and studied their localization. SNARE-binding protein Rop (Wu et al., 1998) exhibited concentrations near ERES-Golgi units, as evidenced by proximity to Golgi marker Grasp65 (Fig. 2 A). Similar to Rop, Vps20, a member of the fly ESCRT-III complex (Vaccari et al., 2009), also concentrated close to ERES-Golgi units (Fig. 2 B). Because the v-ATPase pump, of which VhaPPA1-1 is a component, functions at lysosomes, we examined a possible relation of lysosomes with ERES-Golgi units. To do this, we analyzed lysosomal markers Syntaxin 17 (Syx17) and Lamp1. A GFP-tagged version of Syx17, involved in lysosome fusion events in both *Drosophila* and mammals (Itakura et al., 2012; Takats et al., 2013), formed puncta that seemed to associate (contact or overlap at confocal microscopy resolution) with puncta formed by trans-Golgi markers Golgin245 (antibody staining; Fig. 2 C) and GalT-TagRFP (Fig. 2 D). Furthermore, using an endogenously tagged Lamp1-YFP fusion, we found that Lamp1 puncta frequently lied proximal to both Golgin245 (Fig. 2 E) and GalT (Fig. 2 F). Quantification of their relation revealed Lamp1 puncta near 84.6 ± 3.9% (±SD) of the Golgin245 puncta in fat body, corresponding to 75.1 ± 6.2% of Lamp1 puncta in the cell (Fig. 2 G). Quantification of the relation between Lamp1 and GalT puncta produced similar results (Fig. 2 H). Moreover, we analyzed the position of Lamp1 puncta within ERES-Golgi units and found that they localized trans to the trans-Golgi (Fig. 2 I). These results show that a majority of fat body lysosomes are juxta-trans-Golgi lysosomes, hereafter trans-Golgi–associated (tGA-) lysosomes (Fig. 2 J). Besides fat body, Lamp1 puncta were frequently found proximal to trans-Golgi in all tissues we tested. Percentages of ERES-Golgi units displaying Lamp1 puncta ranged from 53.3 ± 8.6% in wing disc to 77.2 ± 12.3% in midgut (Fig. S2, A and B), suggesting that the vicinity of the trans-Golgi is a predominant location for lysosomes in all fly cell types.

We next wondered about the position of tGA-lysosomes lysosomes in the wider endolysosomal traffic system. A recent study reported that Rab-GTPase Rab11, mediating endosomal recycling, resides frequently near the *Drosophila* trans-Golgi (Fujii et al., 2020a). Besides Rab11, we analyzed the localization of Rab4, Rab5, and Rab7, involved in early recycling, early endosomal, and late endosomal traffic, respectively. Puncta formed by YFP-tagged Rab-GTPases expressed under endogenous regulatory elements (Dunst et al., 2015) frequently located next to trans-Golgi marked with GalT in fat body adipocytes, with Rab11 exhibiting the highest coincidence (Fig. 2, K and L). Imaging of fluorescently tagged versions of these Rab-GTPases expressed under GAL4/UAS control showed similar levels of proximity of Rab4, Rab5, Rab7, and Rab11 with the trans-Golgi (Fig. S2 C). In all four cases, more than half of the puncta located near the trans-Golgi. Altogether, these results indicate that the vicinity of the trans-Golgi is the main cellular station of the fly endolysosomal system.

High-resolution analysis of tGA-lysosomes

To confirm the association of lysosomes with the trans-Golgi, we analyzed the localization of the lysosomal marker Lamp1 within the ERES-Golgi unit using super-resolution structured illumination microscopy (SIM). Lamp1 puncta imaged through SIM were resolvable from trans-Golgi marker GalT (Fig. 3 A), indicating that these structures were distinct from the trans-Golgi. Rab11 localization was similarly resolvable from GalT (Fig. 3 B). We additionally used focused ion beam scanning electron microscopy (FIB-SEM), a technique that allows highly resolved 3D reconstruction of subcellular structures. We recently employed FIB-SEM to characterize the ER–Golgi interface and already noticed frequent presence of lysosomes in ERES-Golgi units (Yang et al., 2021). Re-analyzing these datasets, we found in samples of both fat body (Fig. 3, C and D) and wing disc (Fig. 3 E) that the trans-side of most Golgi complexes displayed spherical or oval-shaped vesicles of 100–300 nm diameter recognizable as lysosomes or lysosome-related degradative bodies due to the presence inside of dark spots and smaller membrane bodies. In total, tGA-lysosomes were present in 68/69 (98.6%) fat body and 54/69 (78.3%) wing disc ERES-Golgi units imaged through FIB-SEM (20 nm *Z*-resolution). tGA-lysosomes sometimes shared a contact area with Golgi membranes similar to the stacking of Golgi cisternae (Fig. 3 F and Video 1). In other cases, tGA-lysosomes lied a short distance from the Golgi without contact (Fig. 3 F and Video 1). Finally, we observed some instances of continuity between tGA-lysosomes and trans-Golgi through narrow connections (Fig. 3, H and I; and Video 1). In ERES-Golgi units reconstructed from FIB-SEM data, tGA-lysosomes found in contact with Golgi were 8/27 (29.6%) in fat body and 4/14 (28.6%) in wing disc, while 19/27 (70.4%) lysosomes in fat body and 10/14 (71.4%) in wing disc lay close but separate from Golgi. In both fat body and wing disc, we observed free lysosomal bodies that were not associated with trans-Golgi (Fig. S3 A). We did not observe late endosomal multivesicular bodies in the L3 feeding stage fat body, although their presence is documented later in L3 wandering stage during programmed autophagy (Maruzs et al., 2015). We did not find double-membrane macroautophagic structures in the L3 feeding fat body either. However, we saw typical multivesicular bodies in wing disc cells, distant from Golgi in most of the cases (16/19; Fig. S3 A). Taken together, these observations confirm the existence of tGA-lysosomes and point to their intimate relation with the trans-Golgi.

In vivo imaging shows association of lysosomes to trans-Golgi is mostly stable

To further characterize the relation between lysosomes and trans-Golgi, we imaged markers for lysosomes (Lamp1-GFP) and trans-Golgi (GalT-TagRFP) in vivo. To do this, we acquired time-lapse movies of blood cells attached to the dorsal epidermis in immobilized larvae using a spinning-disc microscope (Fig. 4, A and B). In total, we imaged 39 blood cells, each for 10 min, at 6-s intervals (Fig. 4 C and Video 2). In these 39 cells, an

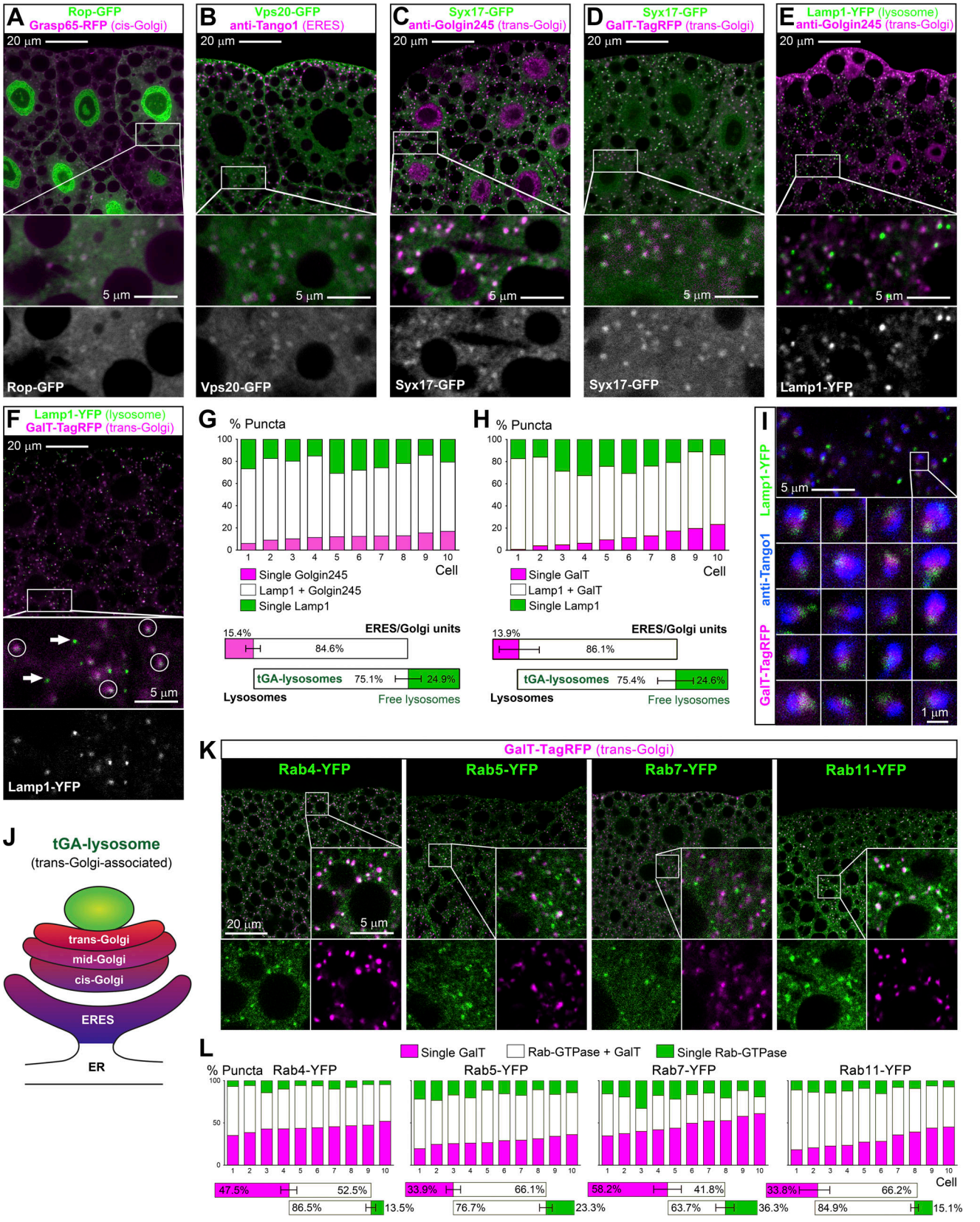

Figure 2. **Juxta-Golgi localization of Rop, Vps20, lysosomal markers, and endosomal Rab-GTPases. (A)** Confocal image of L3 fat body (feeding stage) showing localization of Rop-GFP (green) and cis-Golgi marker Grasp65-RFP (magenta), both driven by *Cg-GAL4*. Magnified insets are shown below for both markers and for Rop alone. **(B)** Localization in fat body of Vps20-GFP (green, driven by *Cg-GAL4*) and ERES Tango1 (antibody staining, magenta). Magnified insets are shown for both markers and Vps20 alone. **(C)** Localization in fat body of Syx17-GFP (green) and trans-Golgi Golgin245 (antibody staining, magenta).

https://doi.org/10.1083/jcb.202203045

Magnified insets show both markers and Syx17 alone. **(D)** Localization in fat body of Syx17-GFP (green) and trans-Golgi marker GalT-TagRFP (magenta), both driven by *BM-40-SPARC-GAL4*. Magnified insets show both markers and Syx17 alone. **(E)** Localization in fat body of Lamp1-YFP (green) and trans-Golgi Golgin245 (magenta). Magnified insets show both markers and Lamp1 alone. **(F)** Localization in fat body of Lamp1-YFP (green) and trans-Golgi GalT-TagRFP (magenta, driven by *BM-40-SPARC-GAL4*). Magnified insets show both markers and Lamp1 alone. Circles and arrows mark examples of tGA- and free lysosomes, respectively. **(G)** Quantification of the proximity between Lamp1-YFP and trans-Golgi Golgin245. The upper graph represents proximity in 10 cells measured in images like those in E. The lower graph represents average proximity values (n = 10, error bars indicate SD): 84.6% of Golgi elements display Lamp1 puncta, while 75.1% of Lamp1 puncta are Golgi-associated. **(H)** Quantification of the proximity between Lamp1-YFP and trans-Golgi GalT-TagRFP as in G, measured in images like those in F. 86.1% of Golgi elements display Lamp1 puncta, while 75.4% of Lamp1 puncta are Golgi-associated. **(I)** Confocal image of fat body showing localization of lysosome marker Lamp1-YFP (green), ERES Tango1 (antibody staining, blue), and trans-Golgi GalT-TagRFP (magenta, driven by *BM-40-SPARC-GAL4*). ERES-Golgi units are shown below at higher magnification. **(J)** Schematic drawing of a *Drosophila* ERES-Golgi unit displaying a tGA-lysosome. **(K)** Confocal images of fat body showing localization of trans-Golgi marker GalT-TagRFP (magenta, driven by *BM-40-SPARC-GAL4*) and endogenously expressed, YFP-tagged Rab-GTPases Rab4, Rab5, Rab7, and Rab11 (green; Dunst et al., 2015). Magnified insets in lower right corner of each image with separate channels below. **(L)** Proximity between trans-Golgi marker GalT-TagRFP and fluorescently tagged Rab-GTPases Rab4, Rab5, Rab7, and Rab11. The upper graphs represent puncta proximity in 10 cells measured in images like those in H. The lower graphs represent average proximity (n = 10, error bars indicate SD).

overwhelming majority of Lamp1 puncta remained stably proximal to trans-Golgi elements during the whole 10-min imaging period (540/561; Fig. 4, D and E). On 20 occasions, we captured Lamp1 puncta detaching from 1 of the 561 trans-Golgi elements imaged (Fig. 4, F and G), while attachment of Lamp1 puncta to trans-Golgi was observed in 17 occasions (Fig. 4, H and I). Finally, we observed events in which Lamp1 puncta detached from trans-Golgi and attached short after to a different trans-Golgi element (six events, Fig. 4, J and K) or the same one (three events, Fig. 4 L). In summary, live animal imaging data documented exchanges between populations of free lysosomes and tGA-lysosomes while at the same time showing that, overall, the association of lysosomes to trans-Golgi is stable.

To further probe the relation of lysosomes and trans-Golgi, we quantified the proximity of Lamp1 and GalT during different stages of mitosis in wing disc cells and found similar levels of proximity between the two markers in mitosis and interphase, suggesting that mitotic disassembly of the Golgi does not affect this relation (Fig. S3 B). We also cultured fat body with secretion inhibitor Brefeldin A (BFA) and actin depolymerizing drug Cytochalasin D, which has been shown to cause disassembly of *Drosophila* Golgi stacks (Kondylis et al., 2007). Neither of these drugs, however, seemed to affect GalT-Lamp1 proximity (Fig. S3, C–E). These data further support a stable relation between trans-Golgi and lysosomes.

Rop acts with Syx1/Syx4 in Rab11-mediated trans-Golgi–to–plasma membrane traffic

The intracellular accumulation of collagen displayed by hits Vps20 and VhaPPA1-1, respectively, an ESCRT component and lysosomal pump subunit, point to defects in late endosomal/lysosomal degradation as the cause for the phenotype. The function of additional hit Rop is less clear in this context. Rop has been shown to function with SNARE Syx1 for neurotransmitter release in *Drosophila* neurons (Wu et al., 1998). Knockdown of Syx1 or closely related SNARE Syx4 (Kloepper et al., 2008) did not cause detectable collagen accumulation (Fig. 5 A). However, simultaneous knockdown of both Syx1 and Syx4 resulted in collagen accumulation and autophagy induction similar to Rop knockdown (Fig. 5, A and B), suggesting that Syx1 and Syx4 may function redundantly. To further investigate this, we generated flies expressing mRFP-tagged Syx1 and Syx4 fusions, and found that they localized to the plasma membrane, with few puncta lying proximal to Golgi (Fig. 5, C and D). Consistent with an interaction of Rop with both Syx1 and Syx4, expression of Syx1-mRFP and Syx4-mRFP strongly recruited Rop-GFP to the plasma membrane, whereas neither Syx7-mRFP, localizing to the plasma membrane as well, nor Syx17-mRFP seemed to modify Rop-GFP localization (Fig. 5, E and F). The same plasma membrane recruitment effect on Rop-GFP was observed using FLAG-HA–tagged fusions of Syx1 and Syx4 (Fig. S4, A and B). Altogether, these data indicate that Syx1/Syx4 function in a traffic route that involves Rop and links the trans-Golgi with the plasma membrane.

While it is possible that Syx1/Syx4 and Rop mediate normal secretory traffic from the trans-Golgi to the plasma membrane, collagen amounts accumulated upon their knockdown were far below those observed for Rab1 or Tango1, blocking secretory transport at the level of the ER–Golgi interface (Fig. S1 C). Moreover, the similar phenotype produced by Vps20 and VhaPPA1-1 knockdown also discourages this interpretation. Therefore, and given the high association of Rab11 with the trans-Golgi, we examined the possibility that Syx1/Syx4 and Rop were required for endocytic recycling linking the trans-Golgi to the plasma membrane. Consistent with this notion, many vesicles positive for Syx1 and Syx4 formed inside cells when we knocked down Rop or Rab11 (Fig. 5, G and H). Conversely, simultaneous knockdown of Syx1 and Syx4, as well as Rop knockdown, produced large amounts of vesicles marked with Rab11 (Fig. 5 I and Fig. S4 C). Additionally supporting a role of Syx1/Syx4 and Rop in Rab11-mediated recycling, knockdown of Rab11 produced intracellular retention of collagen (Fig. 6 A) and autophagy (Fig. 6 B). Examination of recycled endosomal cargo transferrin receptor (TfR-GFP) revealed that 51.7% of trans-Golgi had TfR puncta next to them, these representing 45.1% of the TfR puncta in the cell cytoplasm (Fig. 6, C and D). Upon knockdown of Rab11, TfR-GFP signal disappeared from the plasma membrane and became completely internal, shaped as a combination of thread-like structures and large puncta to which 97.2% of trans-Golgi were proximal (Fig. 6, C and D). Interestingly, when we examined the effect of Rop and Rab11 knockdown, we found a marked increase in the size of the trans-Golgi, labeled with GalT (Fig. 6 E and Fig. S4 D). Furthermore, simultaneous knockdown of Syx1 and Syx4 produced the same effect (Fig. 6 F), confirmed with alternative trans-Golgi marker Golgin245 (Fig. S4, E and F). In contrast, increase in the size of the mid-Golgi, assessed with

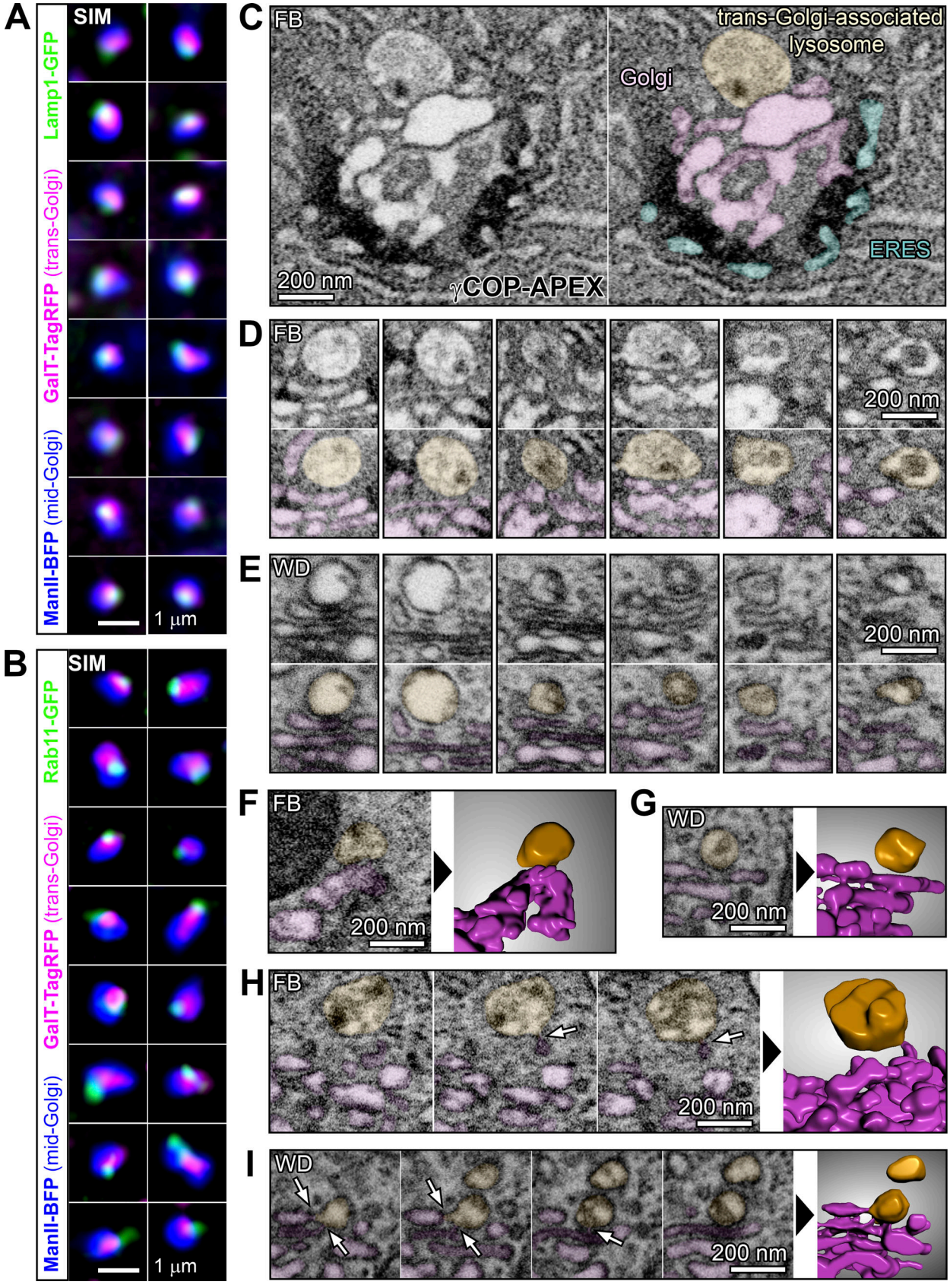

Figure 3. **High-resolution analysis of tGA-lysosomes. (A)** Superresolution (SIM) images of fat body ERES-Golgi units showing trans-Golgi localization of lysosomal marker Lamp1-GFP (green). GalT-TagRFP (trans-Golgi, magenta) and ManII-BFP (mid-Golgi, blue) are shown as well, all driven by *BM-40-SPARC-GAL4*. **(B)** Superresolution (SIM) images of fat body ERES-Golgi units showing trans-Golgi localization of recycling endosome marker Rab11-GFP (green). GalT-

TagRFP (trans-Golgi, magenta) and ManII-BFP (mid-Golgi, blue) are shown as well, *BM-40-SPARC-GAL4*. **(C)** FIB-SEM image of a fat body (FB) ERES-Golgi unit displaying a tGA-lysosome. The same image is pseudocolored on the right side in blue (ERES), purple (Golgi), and yellow (tGA-lysosome). The black staining marks the localization between ERES and Golgi of γCOP (*Cg-GAL4*-driven γCOP-APEX). **(D)** FIB-SEM images featuring examples of tGA-lysosomes in fat body. Superimposed colors in lower images indicate Golgi (purple) and tGA-lysosome (yellow). **(E)** FIB-SEM images featuring examples of tGA-lysosomes in imaginal wing disc (WD). Superimposed colors in lower images as in B. **(F)** FIB-SEM image (left) and reconstructed 3D model (right) of a tGA-lysosome (yellow) sitting on Golgi (purple). Refer to Video 1. **(G)** FIB-SEM image and reconstructed 3D model of a tGA-lysosome (yellow) standing a short distance from Golgi (purple). Refer to Video 1. **(H)** FIB-SEM serial images (left, 20 nm *Z*-distance) and reconstructed 3D model (right) of a tGA-lysosome connected (arrow) to Golgi. Refer to Video 1. **(I)** FIB-SEM serial images (20 nm *Z*-distance) and reconstructed 3D model of a tGA-Golgi lysosome connected (arrows) to Golgi. Refer to Video 1.

the marker ManII, was modest (Rab11 and Rop knockdown) or not significant (Syx1 and Syx4 simultaneous knockdown; Fig. 6, G and H). Altogether, our data show that Rop and Syx1/Syx4 are involved in endocytic recycling, failure of which leads to alterations in the trans-Golgi and trans-Golgi–associated degradative compartment.

Basal autophagy takes place in the trans-Golgi–associated degradative compartment under homeostatic conditions

We next investigated the function of the trans-Golgi–associated degradative compartment in cellular physiology. Because of their abundance, we hypothesized that tGA-lysosomes could be major loci of cellular degradation processes. To test this, we stained adipocytes with an antibody against Ref(2)P, the *Drosophila* ortholog of the p62 autophagic substrate (DeVorkin and Gorski, 2014). Confirming reports by others, we observed Ref(2)P puncta in wild-type fat body adipocytes under normal homeostatic conditions (Pircs et al., 2012). We found that 42.0 ± 8.2% (±SD) of Ref(2)P puncta lied near trans-Golgi, marked with GalT (Fig. 7, A and B). Furthermore, knockdown of autophagy regulator Atg8a not only increased the amount of Ref(2)P in cells, consistent again with findings of others (Pircs et al., 2012), but also caused appearance of large trans-Golgi–proximal Ref(2)P aggregates (Fig. 7 A) and collagen foci (Fig. 7 C), showing the involvement of Atg8a in a basal degradative process affecting both secreted proteins and the Ref(2)P autophagic cargo. Moreover, treatment of adipocytes with autophagy inhibitors Bafilomycin A and chloroquine induced appearance of intracellular Collagen IV puncta as well (Fig. 7 C). In all, these results indicate that juxta-trans-Golgi lysosomes participate in basal autophagic degradation of different cellular materials under normal homeostatic conditions.

The trans-Golgi–associated degradative compartment contributes to the growth of autophagic vesicles in developmental and starvation-induced autophagy

To further characterize the physiological roles of the trans-Golgi–associated degradative compartment, we examined its relation with autophagic vesicles. In fat body adipocytes, developmentally programmed macroautophagy naturally occurs starting in L3 larval wandering stage, after the larva stops feeding, prior to metamorphosis (Rusten et al., 2004). Besides developmental autophagy, autophagic vesicles can be induced in fat body adipocytes by starvation (Scott et al., 2004). We found that nascent autophagic vesicles marked with Atg8a were frequently found proximal to trans-Golgi labeled with GalT in the initial stages of macroautophagy, both developmental (Fig. 8 A) and starvation-induced (Fig. 8 B). Early Atg8a foci seemed to contact or partially overlap GalT in 89.0 ± 4.1% (±SD) and 77.0 ± 5.6% of instances, respectively (Fig. 8, C and D). Furthermore, we observed that both markers more extensively overlapped as autophagic vesicles enlarged (Fig. 8, E and F). In contrast to trans-Golgi GalT, mid-Golgi marker ManII did not become integrated in growing autophagic vesicles (Fig. 8, G and H). Together, these results suggest that in both developmental and starvation-induced autophagy, the trans-Golgi is a main contributor to the growth of autophagic vesicles.

To further investigate the growth of these autophagic vesicles, we examined as well the behavior of ER marker Sec61β. We found in the initial stages of starvation-induced macroautophagy ER membrane concentrations labeled with Sec61β that associated with marker Atg8a in 88.0 ± 9.7% (±SD) of instances (Fig. 9 A). However, these only represented 21.3 ± 10.6% (±SD) of Atg8a puncta, compared to 77.0 ± 5.6% (±SD) that associated with GalT (see Fig. 8 D). More dramatically, during developmental autophagy initiation, no Sec61β puncta were observed at a time when numerous Atg8a puncta had formed (Fig. 9 B). Later, Sec61β concentrations appeared, frequently colocalizing with Atg8, up to the point in the white pupa stage, where 100% of autophagic vesicles contained Sec61β signal (Fig. 9, C and D). Interestingly, we found that knockdown of Atg2, implicated in the formation of autophagosomes from ER (Chowdury et al., 2018; Kotani et al., 2018; Valverde et al., 2019), strongly prevented the incorporation of Sec61β into autophagic vesicles containing Lamp1 (Fig. 9 D). However, this did not affect the incorporation of trans-Golgi GalT (Fig. 9 E) or the formation of mature autolysosomes similar to the ones formed in the wild type according to TEM images (Fig. 9 F). Altogether, these data confirm that ER membranes are incorporated into *Drosophila* autophagic vesicles but question an absolute requirement in their formation or a major contribution to their growth.

To finally confirm the contribution of the secretory pathway to autophagic vesicle growth, we tested the requirement of different Rab-GTPase traffic regulators. To do this, we measured the diameter of autophagic vesicles in the fat body in the white pupa stage (0–1 h after the onset of metamorphosis). Knockdown of Rab5 and Rab7, mediating early and late endosomal traffic, respectively, decreased the diameter of autophagic vesicles labeled with Lamp1 or Atg8a (Fig. 10, A–C), consistent with the contribution of endocytic membranes that others have shown in the same system (Hegedűs et al., 2016; Hennig et al., 2006). We observed a similarly strong decrease in the size of autophagic vesicles when we expressed a dominant negative form of ER–Golgi secretion regulator Rab1 (Fig. 10, A–C), indicating a strong requirement of secretory traffic as well. Other ER–Golgi traffic regulators affecting vesicle size were RabX3 (also known as

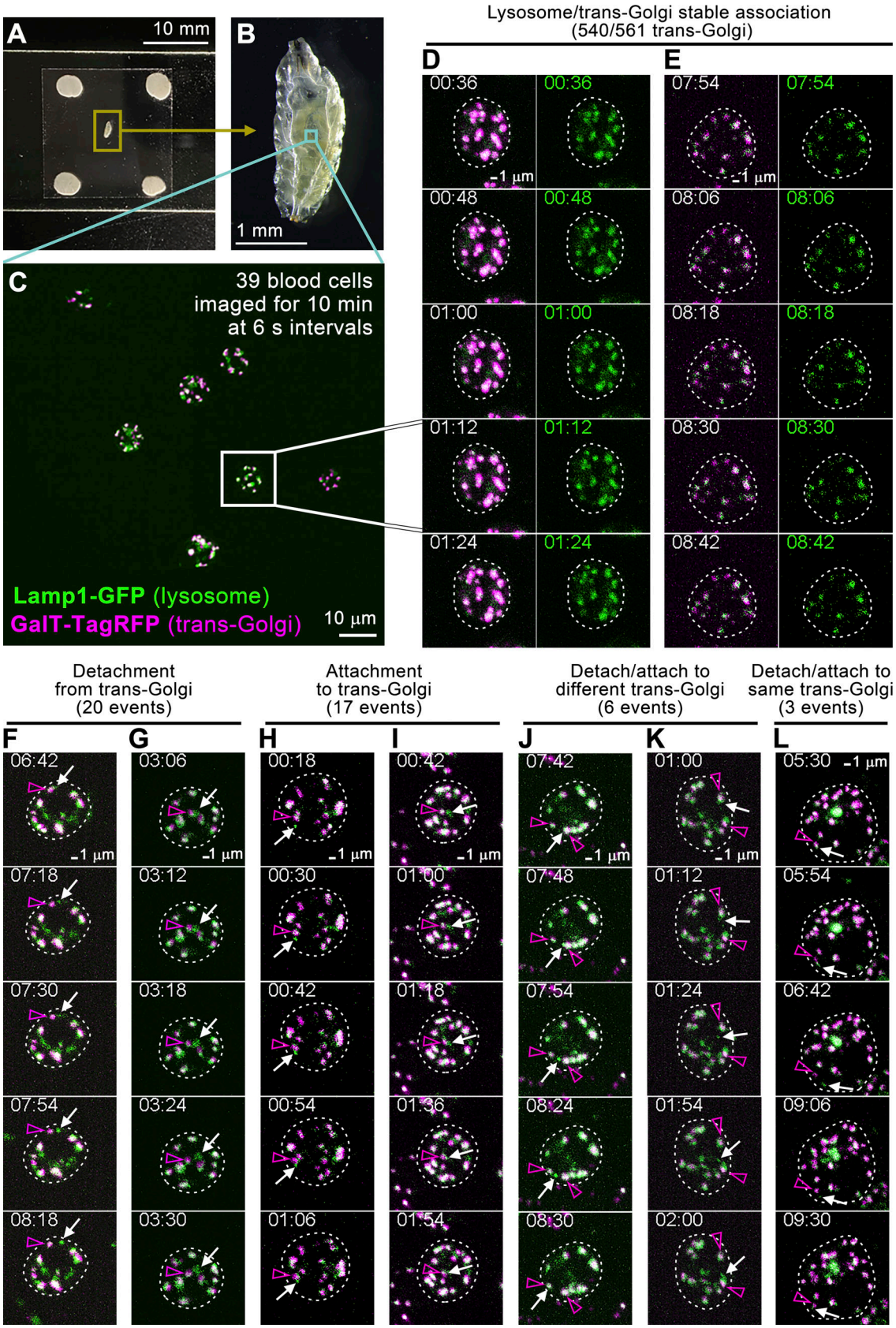

Figure 4. **In vivo imaging shows association of lysosomes to trans-Golgi is mostly stable. (A)** Setup for in animal imaging of blood cells. An L3 larva is shown immobilized between a glass slide and a coverslip held together by modeling clay. **(B)** Higher magnification image of the larva in A. **(C)** Spinning-disc confocal image of live blood cells expressing lysosomal marker Lamp1-GFP (green) and trans-Golgi marker GalT-TagRFP (magenta), both driven by *BM-40-*

SPARC-GAL4. 39 cells were recorded for 10 min each at a speed of 10 images/min. Each image is a maximum intensity projection of a 7–9 section stack (*z*-distance 1 µm). **(D)** Still images from a spinning-disc confocal recording of a live blood cell expressing lysosomal marker Lamp1-GFP (green, shown separately on the right) and trans-Golgi marker GalT-TagRFP (magenta). Lysosomes are stably associated with trans-Golgi. Refer to Video 2. **(E)** Still images from a recording of a blood cell as in D. **(F)** Still images from a live blood cell as in D. A lysosome (white arrow) is seen detaching from trans-Golgi (magenta arrowhead). Refer to Video 2. **(G)** Lysosome detaching from trans-Golgi as in F. **(H)** Still images from a live blood cell as in D. A lysosome (white arrow) is seen attaching to trans-Golgi (magenta arrowhead). Refer to Video 2. **(I)** Lysosome attaching to trans-Golgi as in H. **(J)** Still images from a live blood cell as in D. A lysosome (white arrow) is seen detaching from a trans-Golgi element and attaching to a different one (magenta arrowheads). Refer to Video 2. **(K)** Lysosome detaching from a trans-Golgi element and attaching to a different one as in J. **(L)** Still images from a live blood cell as in D. A lysosome (white arrow) is seen detaching from a trans-Golgi element (magenta arrowhead) and re-attaching to it. Refer to Video 2.

Rab9Fb; Ke et al., 2018), decreasing the size of autophagic vesicles, and Rab2, remarkably increasing it (Fig. 10, B and C). Finally, knockdown of Rab6 and Rab10, involved in traffic and sorting at the fly trans-Golgi (Ayala et al., 2018; Lerner et al., 2013; see localization in Fig. S5) significantly decreased autophagic vesicle size (Fig. 10, B and C). Taken together, our results lead us to conclude that the convergence of secretory and endosomal traffic not only gives rise to a trans-Golgi–associated degradative compartment in homeostatic conditions but also contributes to autophagic vesicle growth upon macroautophagy induction (Fig. 10 D).

Discussion

In this study, we found that the vicinity of the trans-Golgi is the major subcellular location for lysosomes in the *Drosophila* fat body and other tissues. Through animal imaging, we found that tGA-lysosomes and free lysosomes are dynamic and interconvertible. Nonetheless, the scarcity of these exchanges indicates that the association between lysosomes and trans-Golgi is relatively long-lived. Supporting this, electron microscopy imaging of tGA-lysosomes revealed sometimes extensive areas of contact and occasional membrane connections with trans-Golgi cisternae. Further research is needed to ascertain whether tGA-lysosomes and free lysosomes are functionally different or equivalent populations in terms of their properties and traffic relations. Lysosomes in human cells can be found throughout the cytoplasm, but significantly concentrate near the nucleus and the centrosomal microtubule organizing center, suggesting a relation with the juxtanuclear Golgi, located there as well (Pu et al., 2016). It remains to be investigated whether a close Golgi–lysosome relation as seen in *Drosophila* is found as well in human cells.

Besides lysosomes, our study revealed close physical proximity of the whole endolysosomal system near the trans-Golgi. Rab-GTPase regulators of endosomal traffic Rab4, Rab5, Rab7, and Rab11 frequently located there. Among these, Rab11 (recycling endosome) exhibited the highest degree of trans-Golgi association, consistent with recent studies showing that Rab11 foci attach to the trans-side of Golgi stacks in *Drosophila*, sea urchin, and human cells (Fujii et al., 2020a; Fujii et al., 2020b). Similar to our observations of tGA-lysosomes in live blood cells, imaging in the *Drosophila* S2 cell line showed most trans-Golgi elements continuously accompanied by recycling endosomes that occasionally attached or detached (Fujii et al., 2020a). Our findings are partly reminiscent as well of the early GERL (Golgi–ER–lysosome) hypothesis: the proposal, based on electron microscopy observations in mammalian cells, that lysosomes arises from a juxta-trans-Golgi membrane system continuous with the ER (Novikoff and Novikoff, 1977). Later, as data failed to support ER–lysosome continuity, the GERL hypothesis was abandoned in favor of the current TGN model. However, our observations of a close relation between trans-Golgi and lysosomes, together with modern evidence of ER–endolysosomal contact sites (Klumperman and Raposo, 2014), advise revisiting the GERL concept.

Our results are reminiscent as well of the situation in budding yeast and plant cells. *Saccharomyces cerevisiae* has a minimal endomembrane system where the TGN serves as both an early and recycling endosome, with Rab11 homolog Ypt31 localizing there as well (Day et al., 2018). Similarly, in plants, endocytic and secretory traffic routes meet in a TGN/early endosome hybrid organelle (Robinson, 2020; Viotti et al., 2010). Lysosomal-like degradation in yeast and plants, however, takes place separately in the vacuole, which does not associate with the TGN but with a distinct prevacuolar compartment that combines properties of both early and late endosomes (Day et al., 2018; Hu et al., 2020; Nagano et al., 2019). Interestingly, plant v-ATPases are known to function in both the vacuole and TGN (Luo et al., 2015). Further analysis with a wider phylogenetic perspective may help understand the evolutionary implications of these findings for the evolution of the endomembrane system. We speculate that an ancestral situation could have seen the trans-Golgi as the main or single interface concentrating all eukaryotic endosomal, degradative, and secretory traffic routes.

Our findings offer a renewed spatial framework for integrating multiple pieces of evidence that point to a particularly strong connection between the secretory and endolysosomal systems in *Drosophila*. For instance, early, late, and recycling endosomal traffic are all required for the formation and maturation of secretory glue granules in larval salivary glands (Burgess et al., 2012; Ma and Brill, 2021; Ma et al., 2020; Neuman et al., 2021a; Neuman et al., 2021b). Also in salivary glands, excess secretory glue granules are known to fuse with lysosomes for degradation in an autophagic process (crinophagy) requiring Rab7 and Rab2 (Csizmadia et al., 2018). Furthermore, requirements in macroautophagy have been shown for Golgi-localized proteins Ema (Kim et al., 2012), Rab2 (Fujita et al., 2017; Gotz et al., 2021; Lőrincz et al., 2017; Lund et al., 2018), and Rab6 (Ayala et al., 2018). The convergence of early, late, and recycling endosomes with lysosomes and secretory membranes in the *Drosophila* trans-Golgi raises questions on how spatial and functional segregation of trafficking routes and compartments can be achieved in such a reduced space. Recently, segregation of

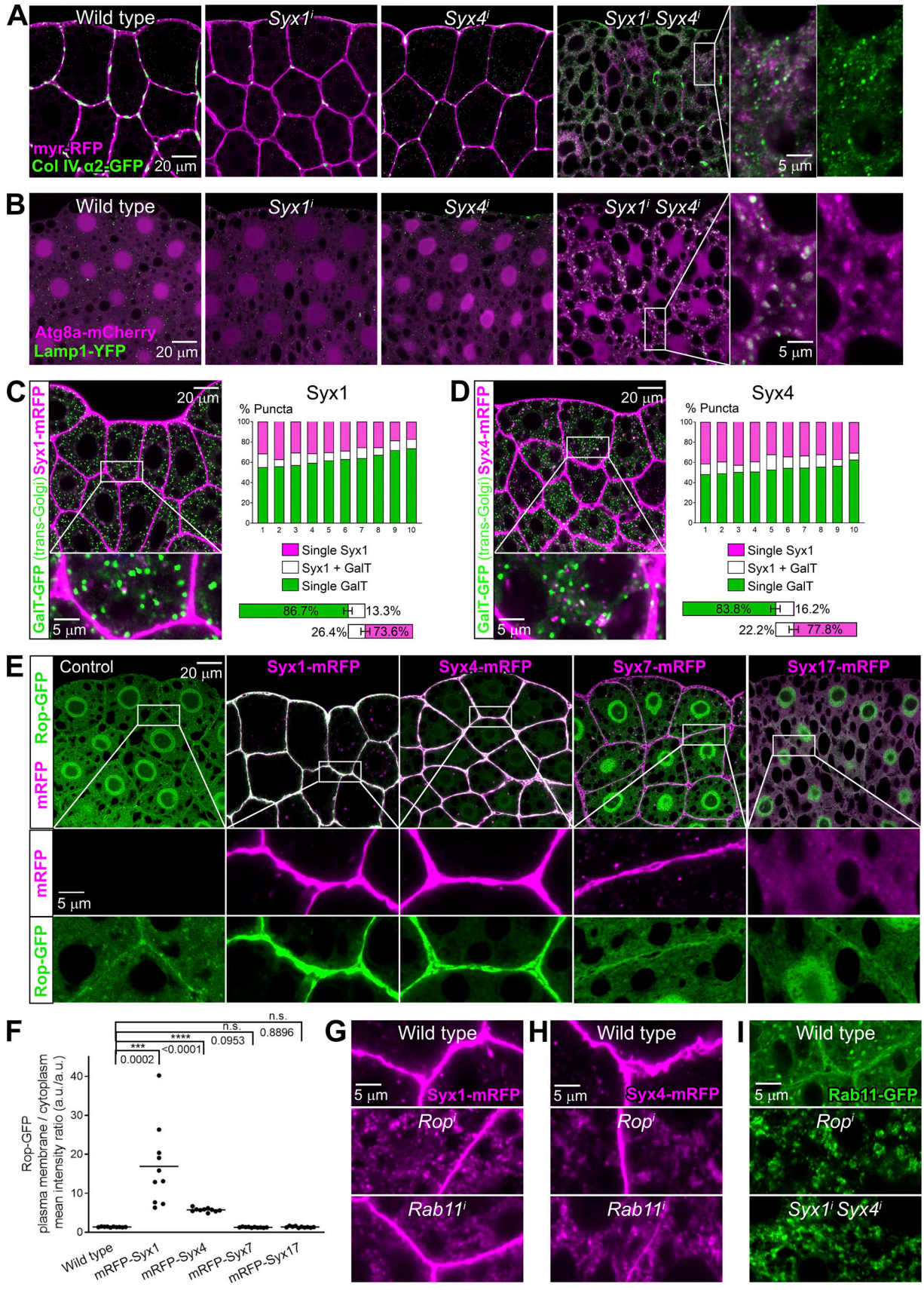

Figure 5. **Rop acts with Syx1/Syx4 in trans-Golgi-to–plasma membrane recycling. (A)** Confocal images of fat body from wild-type, *BM-40-SPARC>Syx1^{i}*, *>Syx4^{i}* and double *>Syx1^{i}+Syx4^{i}* L3 larvae (feeding stage) showing localization of Collagen IV (α2 chain Vkg-GFP, green). Plasma membrane labeled with *BM-40-*

SPARC-GAL4–driven myr-RFP (magenta). Magnified inset shows intracellular Collagen IV accumulation in >*Syx1*^{i}+*Syx4*^{i} fat body, with the Collagen IV channel separated on the right. **(B)** Fat body from wild-type, *BM-40-SPARC*>*Syx1*^{i}, >*Syx4*^{i}, and >*Syx1*^{i}+*Syx4*^{i} larvae showing markers Lamp1-YFP (lysosomes, green) and Atg8a-mCherry (autophagosomes, magenta). Plasma membrane labeled with *BM-40-SPARC-GAL4*–driven myr-RFP (magenta). Magnified inset shows formation of autophagic vesicles in >*Syx1*^{i}+*Syx4*^{i} fat body, with the Atg8a channel separated on the right. **(C)** Fat body showing localization of Syx1-mRFP (magenta) and trans-Golgi marker GalT-GFP (green), both driven by *Cg-GAL4*. The graphs on the right quantify their proximity in 10 individual cells (upper graph) and average proximity (lower graphs, *n* = 10, error bars indicate SD). **(D)** Fat body showing localization of mRFP-Syx4 (magenta) and trans-Golgi marker GalT-GFP (green), both driven by *Cg-GAL4*. The graphs quantify their proximity as in C. **(E)** Fat body expressing Rop-GFP alone (control) or co-expressing Rop-GFP with Syx1-mRFP, Syx4-mRFP, Syx7-mRFP, and Syx17-mRFP, all driven by *BM-40-SPARC-GAL4*. GFP in green and mRFP in magenta. Rectangular insets are shown magnified below. **(F)** Quantification of the recruitment of Rop-GFP to the plasma membrane by Syx1, Syx4, Syx7, and Syx17. Each dot represents the ratio of Rop-GFP intensity between plasma membrane and cytoplasm in one cell, measured in images like those in E. *n* = 10. Horizontal lines mark the mean. P values from unpaired *t* tests for differences with the control are reported. n.s., P > 0.05; ***, 0.001 > P > 0.0001, and ****, P < 0.0001. **(G)** Localization of Syx1-mRFP (magenta) in wild-type, *Cg* >*Rop*^{i}, and >*Rab11*^{i} fat body. **(H)** Localization of Syx4-mRFP (magenta) in wild-type, *Cg*>*Rop*^{i}, and >*Rab11*^{i} fat body. **(I)** Localization of Rab11-GFP (green) in wild-type, *BM-40-SPARC*>*Rop*^{i}, and >*Syx1*^{i}+*Syx4*^{i} fat body.

distinct secretory and vacuolar cargo sorting zones has been demonstrated through in vivo imaging in the TGN of plant cells (Shimizu et al., 2021), suggesting that stringent sorting mechanisms must be at play to separate the secretory and degradative routes. An alternative explanation is that perhaps proteins destined for secretion do in fact traffic through the trans-Golgi–associated degradative compartment while protected from degradation through a mechanism yet to be determined.

Beyond endolysosomal degradation, we found that tGA-lysosomes function in basal autophagy. We observed Ref(2)P autophagic cargo in the trans-Golgi–associated degradative compartment in normal conditions. Also, secretory cargo (Collagen IV and general secretion marker secr-GFP) accumulated when the function of this compartment was compromised, revealing crinophagic degradation similar to salivary glands (Csizmadia et al., 2018). Because no macroautophagic structures or double isolation membranes were seen in electron microscopy, we conclude that this basal autophagy occurs directly in lysosomes. Our data, nonetheless, show that the canonical macroautophagic cascade component Atg8a must be involved. Indeed, presence of Atg8a in microautophagic endosomes has been shown in starvation-induced microautophagy in the fat body (Mukherjee et al., 2016). Besides Atg8a, loss of function of other Atg cascade components produces accumulation of Ref(2)P in fat body cells of the feeding larva (Pircs et al., 2012), evidence also of their involvement in basal autophagy, probably in a non-canonical role. Also consistent with a basal microautophagic process are the requirements of ESCRTIII component Vps20 and v-ATPase subunit VhaPPA1-1. Loss of v-ATPase, essential for lysosomal function, and ESCRT, required for microautophagic vesicle ingression into lysosomes (Oku et al., 2017; Zhu et al., 2017), are known to trigger macroautophagy in *Drosophila* (Mauvezin et al., 2015; Rusten et al., 2007). We therefore propose that disruption of basal microautophagy in which they are involved triggers compensatory macroautophagy due to decreased autophagic flux.

In addition to lysosome (VhaPPA1-1) or late endosome (Vps20) dysfunction, our characterization of the third hit Rop revealed that failure of endocytic recycling disrupts the trans-Golgi–associated degradative compartment and triggers macroautophagy as well. Our data show that Rop interacts with both Syx1 and Syx4, and their loss produced accumulation of Rab11-positive vesicles. Conversely, Rab11 loss caused accumulation of Syx1/4-positive vesicles. Further supporting an involvement of Rop and Syx1/Syx4 in endocytic recycling from the trans-Golgi to the plasma membrane, knockdown of Rab11 itself caused autophagy, collagen accumulation and enlargement of the trans-Golgi. Of note, a previous study in the salivary gland showed decreased formation of acidic vacuoles during programmed cell death upon loss of Rab11, Syx1, and Syx4 (Farkas et al., 2015), linking Syx1 and Syx4 to endocytic recycling like our study. Importantly, our data indicate that defects in endosomal routes can indirectly affect secretion at the trans-Golgi by disrupting compartments that are physically linked or close. In this context, it is worth reexamining early claims that Rab11 (Chen et al., 1998), dynamin (Jones et al., 1998; Kreitzer et al., 2000), or clathrin (Fölsch et al., 1999) are involved in still elusive Golgi-to–plasma membrane secretory transport.

Finally, our characterization of tGA-lysosomes revealed increasing association with Atg8a foci during developmental and starvation-induced autophagy. Our findings are consistent with a scenario in which autophagosomes formed elsewhere move to fuse with the trans-Golgi–associated degradative compartment upon macroautophagy induction. The effects on autophagic vesicle size of Rab1 loss, blocking ER–Golgi traffic, were comparable to those of endosomal Rab5 and Rab7, indicating a strong requirement for secretory pathway membranes in autophagic vesicle growth. Strikingly, Rab2 knockdown increased, rather than decreased, autophagic vesicle size, pointing to an involvement in retrograde Golgi–ER traffic opposed to Rab1, although a function has been assigned to *Drosophila* Rab2 in trans-Golgi traffic as well (Gotz et al., 2021). Significant effects were seen as well when we knocked down trans-Golgi–localized Rab6 and Rab10, proving contributions from trans-Golgi traffic. Involvement of other Golgi membranes is possible, but likely a later event, as trans-Golgi GalT associates with autophagic vesicles when mid-Golgi ManII does not. Interestingly, knockdown of Atg2 prevented the incorporation of the ER marker Sec61β into autophagic vesicles, but autolysosomes formed in this condition seemed normal, calling into question an absolute requirement of *Drosophila* Atg2 in autophagosome formation from ER membranes. Further research is needed, therefore, to unravel the temporal order and relative contributions of different membrane compartments to autophagic vesicle growth, including the source of the initial autophagosomes. Future work in *Drosophila* could ascertain more details of autophagic vesicle formation by combining ultrastructural observations, functional genetic experiments and in vivo imaging. Nonetheless, our findings here

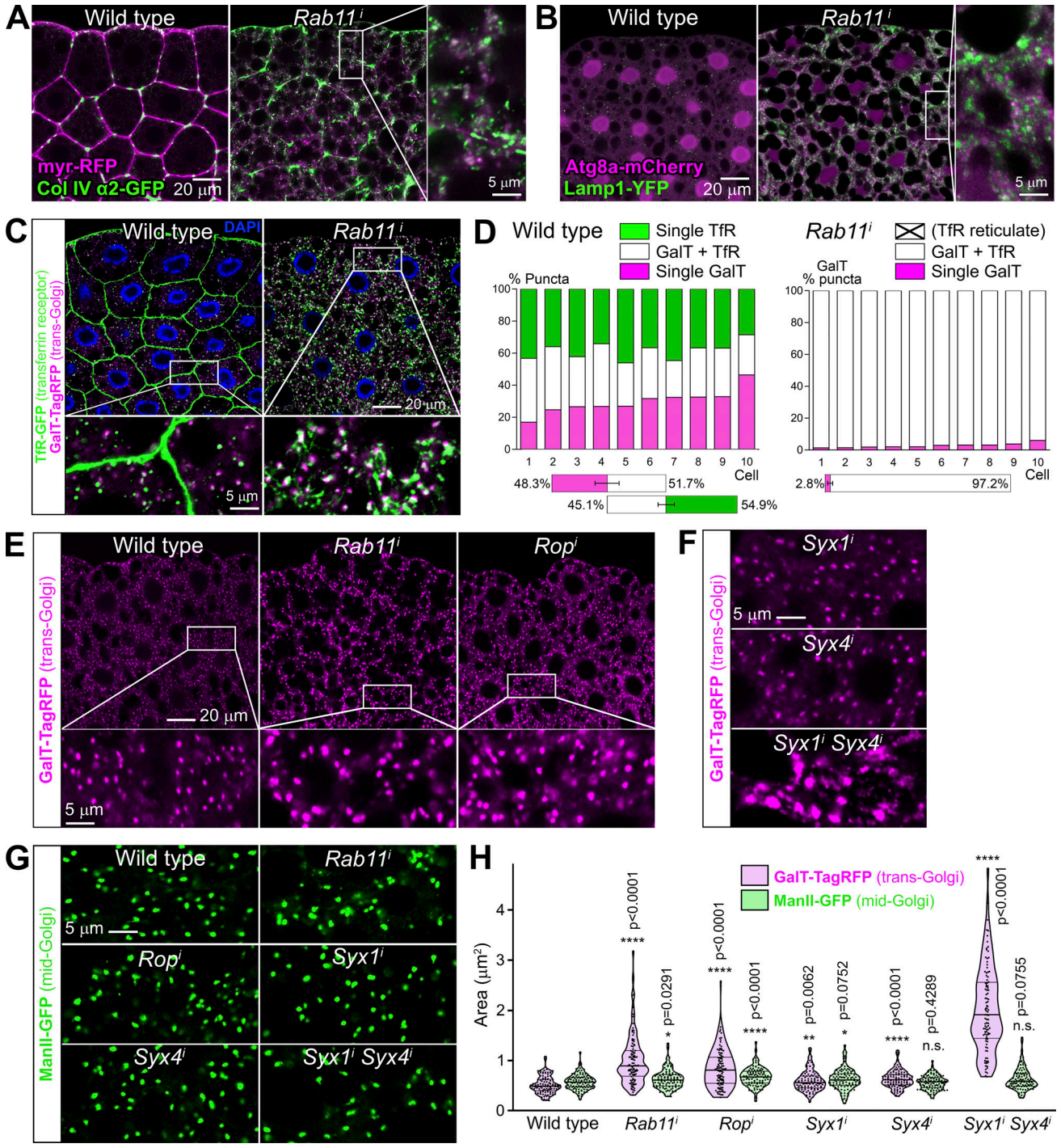

Figure 6. **Endocytic recycling block leads to secretory cargo retention, autophagy, and trans-Golgi enlargement. (A)** Confocal images of fat body from wild-type and *BM-40-SPARC>Rab11*^{i} L3 larvae (feeding stage) showing intracellular accumulation of Collagen IV (α2 chain Vkg-GFP, green). Plasma membrane labeled with myr-RFP (magenta). Rectangular inset magnified on the right side. **(B)** Fat body from wild-type and *BM-40-SPARC>Rab11*^{i} larvae showing autophagic vesicle formation (Atg8a-mCherry in magenta; Lamp1-YFP in green). Rectangular inset magnified on the right side. **(C)** Wild-type and *Cg>Rab11*^{i} fat body expressing trans-Golgi marker GalT-TagRFP (magenta) and endocytic marker TfR-GFP (green). Upon Rab11 knockdown, TfR signal disappears from the plasma membrane and forms larger puncta connected by thread-like structures. Rectangular insets are shown magnified below. **(D)** Quantification of the proximity between TfR-GFP and GalT-TagRFP. The upper graph represents proximity in 10 cells measured in images like those in C. The lower graph represents average proximity values (n = 10, error bars indicate SD). 51.7% of trans-Golgi are proximal to TfR puncta in the wild type. Upon Rab11 knockdown, 97.2% of Golgi are proximal to TfR-positive structures (note that TfR signal could not be analyzed as individual puncta in this condition). **(E)** Wild-type, *BM-40-SPARC>Rab11*^{i}, and *>Rop*^{i} fat body expressing trans-Golgi marker GalT-TagRFP (magenta). Rectangular insets are shown magnified below. **(F)** *BM-40-SPARC>Syx1*^{i}, *>Syx4*^{i} and double *>Syx1*^{i}*+Syx4*^{i} fat body expressing trans-Golgi marker GalT-TagRFP (magenta). **(G)** Wild-type, *BM-40-SPARC>Rab11*^{i}, *>Rop*^{i}, *>Syx1*^{i}, *>Syx4*^{i}, and double *>Syx1*^{i}*+Syx4*^{i} fat body expressing mid-Golgi marker ManII-GFP (green). **(H)** Trans-Golgi and mid-Golgi size measured in images like those in E–G. The data are presented as violin plots where quartiles are marked, with dots representing individual measurements of punctum size. n = 100. P values from unpaired t tests are indicated for differences with the wild type. n.s., P > 0.05; *, 0.05 > P > 0.01; **, 0.01 > P > 0.001; ****, P < 0.0001.

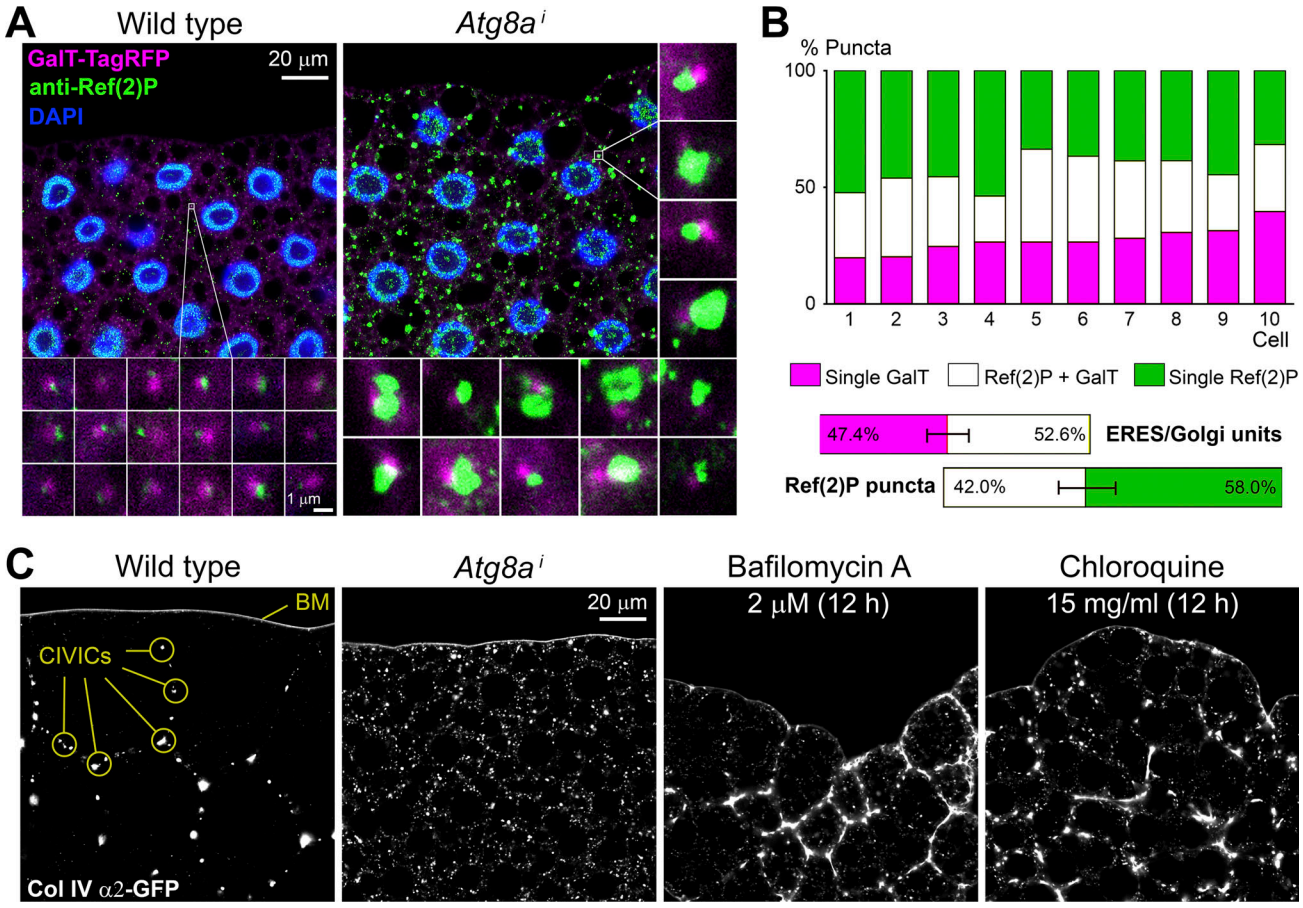

Figure 7. **Basal autophagy takes place in the trans-Golgi–associated degradative compartment under homeostatic conditions. (A)** Confocal images of L3 fat body (feeding stage) from wild-type (left) and *BM-40-SPARC>Atg8a*^{i} (right) larvae showing localization of autophagic cargo Ref(2)P (antibody staining, green) and trans-Golgi marker GalT-TagRFP (magenta, driven by *BM-40-SPARC-GAL4*). Examples of Ref(2)P puncta proximal to trans-Golgi are shown at higher magnification. Nuclei in blue (DAPI). **(B)** Proximity between Ref(2)P and GalT-TagRFP in wild-type fat body. The upper graph represents proximity measured in 10 cells. The lower graph represents average proximity values (n = 10, error bars indicate SD). **(C)** Localization of Collagen IV (α2 chain Vkg-GFP) in L3 fat body (feeding stage) from wild type (left), *BM-40-SPARC>Atg8a*^{i} (center left), and wild type treated for 12 h with autophagy inhibitors Bafilomycin A (2 µM, center right) and chloroquine (15 mg/ml, right). Collagen IV puncta in the wild type correspond not to intracellular accumulation, but to CIVICs (see Fig. 1 A). BM indicates basement membrane.

already demonstrate that the fly trans-Golgi is the major cellular traffic hub in this animal and that convergence of secretory, endosomal, and degradative pathways there determines endomembrane organization in both normal and stress conditions.

Materials and methods

Drosophila husbandry

Standard fly husbandry techniques and genetic methods were used to cross strains and evaluate segregation of transgenes in the progeny of crosses (Roote and Prokop, 2013). The GAL4-UAS binary expression system (Brand and Perrimon, 1993) was used to drive expression of UAS transgenes under control of GAL4 drivers *BM-40-SPARC-GAL4* (fat body), *Cg-GAL4* (fat body), *rn-GAL4* (wing disc), and *actin-GAL4* (ubiquitous). Stable insertion of transgenic UAS constructs was achieved through standard P-element transposon transgenesis (Rubin and Spradling, 1982). Flies were cultured on standard fly food containing 24.5 g/liter yeast, 50 g/liter cornmeal, 30 g/liter brown granulated sugar, 7.25 g/liter white granulated sugar, 10 g/liter agar, 4 ml/liter propionic acid, 1.75 g/liter methyl-4-hydroxybenzoate, and 17.5 ml/liter absolute alcohol. Fly cultures were maintained at 25°C, except for experiments using the thermosensitive GAL4 repressor GAL80^{ts} (Fig. S1 C; McGuire et al., 2003), in which larvae were kept at 18°C for 4 d followed by transfer of cultures to 30°C for 2 d to initiate GAL4/UAS-driven knockdown. For starvation assays (Fig. 8, B, D, F and H; and Fig. 9 A), late L3 feeding larvae were let to float for 3 or 6 h on plates with PBS containing 20% sucrose prior to dissection. Genotypes of animals in all experiments are detailed in Table S1. Strains used were as follows: *w*^{1118} (BDSC_3605); *w ; vkg*^{G454}*-GFP/CyO ; BM-40-SPARC-GAL4 UAS-Dcr2/TM6B* (Zang et al., 2015); *w ; UAS-myr-RFP/CyO* (BDSC_7118); *w ; UAS-Dcr2* (III) (BDSC_24651); *w ; UAS-Rop.RNAi* $^{VDRC.v19696}$*/(TM3)* (VDRC_v19696); *y v ; UAS-Vps20.RNAi* ^{THU5269}*/(CyO)* (THFC_THU5269); *y v sc ; UAS-VhaPPA1-1.RNAi* $^{TH04233.N}$*/(CyO)* (THFC_TH04233.N); *w ; UAS-secr-GFP* (II) (Pfeiffer et al., 2002); *y w ; UAS-mCherry-Atg8a ; Dr/TM3, Ser* (BDSC_37750); *w ; Cg-GAL4* (II) (BDSC_7011); *w ; UAS-Rop-GFP-2-12* (III) (this study);

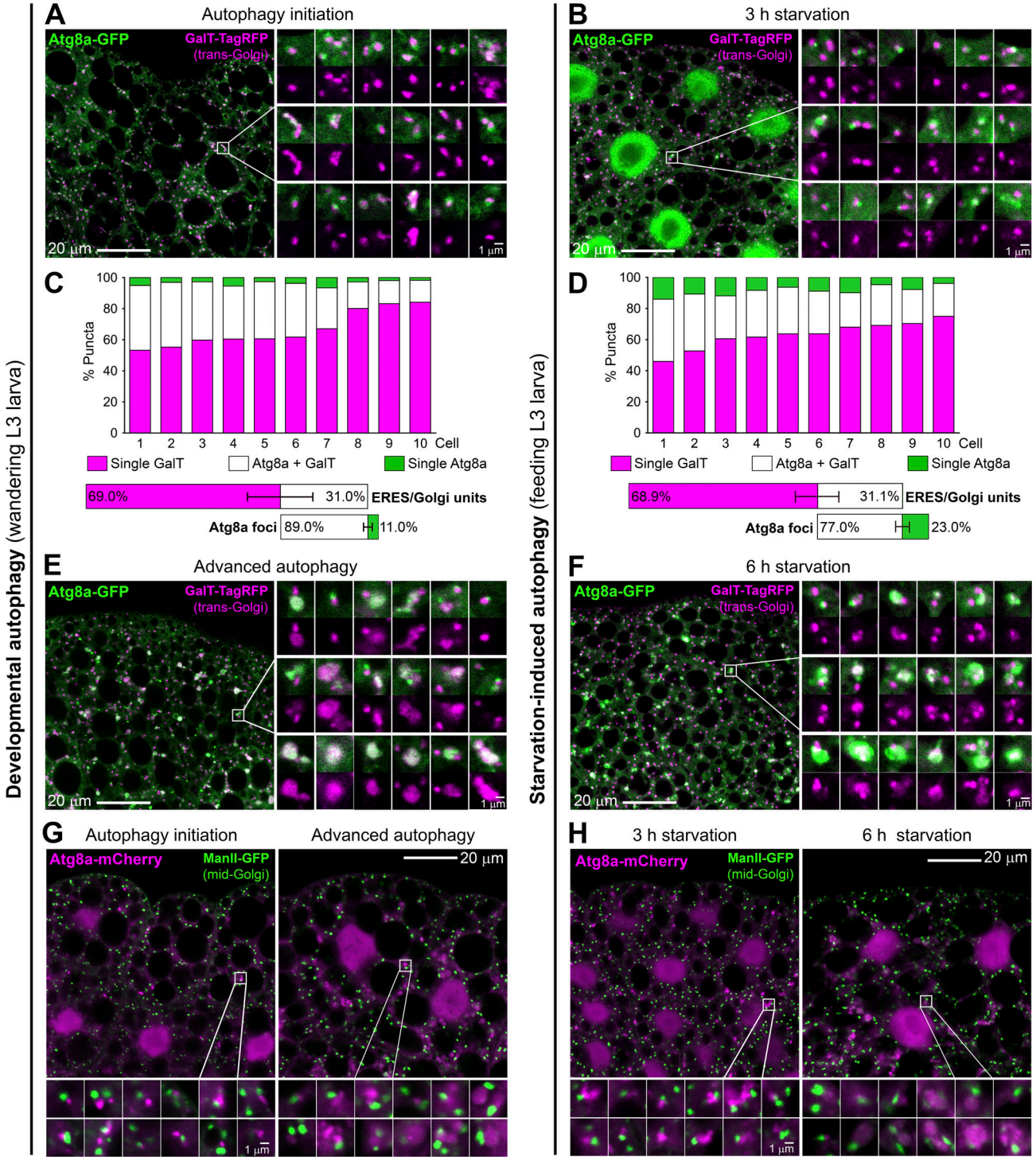

Figure 8. **The trans-Golgi–associated degradative compartment contributes to autophagic vesicle growth during developmental and starvation-induced autophagy. (A)** Confocal image of L3 fat body (wandering stage) showing autophagic marker Atg8a-GFP (green) and trans-Golgi marker GalT-TagRFP (magenta), both driven by *BM-40-SPARC-GAL4*. During the wandering stage, adipocytes initiate programmed autophagy prior to metamorphosis. Examples of nascent autophagic vesicles are shown on the right side at higher magnification. **(B)** Atg8a-GFP (green) and GalT-TagRFP (magenta) in fat body starved for 3 h. Nascent autophagic vesicles on the right side. **(C)** Proximity between Atg8a-GFP and GalT-TagRFP in fat body initiating programmed autophagy, measured in images like those in A. The upper graph represents proximity in 10 individual cells. The lower graph represents average proximity values (n = 10, error bars indicate SD): 89.0% of Atg8a puncta are trans-Golgi–associated. **(D)** Proximity between Atg8a-GFP and GalT-TagRFP in fat body starved for 3 h, measured in images like those in B. The upper graph represents proximity in 10 cells. The lower graph represents average proximity values (n = 10, error bars indicate SD). **(E)** Fat body in advanced programmed autophagy phase showing localization of Atg8a-GFP (green) and GalT-TagRFP (magenta). Growing autophagic vesicles are shown on the right side. **(F)** Fat body starved for 6 h showing localization of Atg8a-GFP (green) and GalT-TagRFP (magenta). Growing autophagic vesicles are shown on the right side. **(G)** Fat body in initial (left) and advanced (right) phases of programmed autophagy showing localization of Atg8a-mCherry (magenta) and mid-Golgi marker ManII-GFP (green), both driven by *BM-40-SPARC-GAL4*. Growing autophagic vesicles are shown below at higher magnification.

Notice that ManII, unlike GalT, does not ingress into autophagic vesicles. **(H)** Atg8a-mCherry (magenta) and ManII-GFP (green) in fat body starved for 3 h (left) and 6 h (right). Growing autophagic vesicles are shown below.

w ; UAS-Grasp65-RFP-3-1 (III) (Yang et al., 2021); *w ; UAS-Vps20-GFP-3-8* (II) (this study); *w ; UAS-GFP-Syx17-19-2/CyO* (this study); *w ; Lamp1^{CPTI001775}-YFP/(CyO)* (DGGR_115240); *w ; UAS-GalT-TagRFP ; TM2/TM6B, Tb* (BDSC_65251); *y w ; UASp-YFP-Rab4* (II) (BDSC_23269); *w ; UAS-GFP-Rab5/CyO* (Wucherpfennig et al., 2003); *w ; UAS-GFP-Rab7* (III) (BDSC_42706); *w ; UAS-Rab11-GFP* (II) (BDSC_8506); *w ; UAS-ManII-EBFP* (III) (BDSC_65250); w ; *UAS-γCOP-APEX-GFP-3-1* (Yang et al., 2021); *w ; UAS-GFP-Lamp1/(CyO)* (BDSC_42714); *w ; UAS-mRFP-Syx1-19-3* (III) (this study); *w ; UASp-GFP-GalT* (II) (BDSC_31422); *w ; UAS-mRFP-Syx4-19-2* (III) (this study); *w ; UAS-mRFP-Syx7-2-1* (III) (this study); *w ; UAS-mRFP-Syx17-4-1* (III) (this study); *w ; Sco/CyO ; UAS-hTfR.DeltaC.GFP* (III) (BDSC_36859); y *v ; UAS-Rab11.RNAi^{THU2817}* (III) (THFC_THU2817); *w ; UAS-Rop.RNAi$^{VDRC.v106242}$* (II) (VDRC_v106242); *y v ; UAS-Syx1.RNAi^{THU2029}* (III) (THFC_THU2029); *y sc v sev ; UAS-Syx4.RNAi^{THU5572}/CyO* (THFC_THU5572); *w ; UAS-ManII-EGFP ; TM2/TM6B, Tb* (BDSC_65248); *w ; UAS-Atg8a.RNAi ^{THU2899}, e/TM3, Sb* (THFC_THU2899); *hs-FLP y w ; UAS-Atg8a-GFP* (II) (BDSC_52005); *w ; UAS-tdTomato-Sec61β* (III) (BDSC_64747); *y v sc ; UAS-Atg2.RNAi$^{TRiP.JF02786}$* (III) (BDSC_27706); *y sc v sev ; UAS-Rab5.RNAi $^{TRiP.HMS00147}$* (III) (BDSC_34832); *y v ; UAS-Rab7.RNAi $^{TRiP.JF02377}$* (III) (BDSC_27051); *w ; UAS-mRFP-Rab1^{DN}* (II) (this study); *w ; UAS-YFP-Rab1^{DN}* (III) (BDSC_9757); *y sc v sev ; UAS-Rab2.RNAi^{THU1506}* (III) (THFC_THU1506); *y v ; UAS-Rab6.RNAi $^{TRiP.JF02640}$* (III) (BDSC_27490); *y sc v sev ; UAS-Rab9.RNAi^{THU4458}* (II) (THFC_THU4458); *y v ; UAS-Rab10.RNAi $^{TRiP.JF02058}$* (III) (BDSC_26289); *y sc v sev ; UAS-RabX3.RNAi^{THU1589}* (III) (THFC_THU1589); *w ; UAS-Tango1.RNAi $^{VDRC.v21594}$/TM3* (VDRC_v21594); *y v ; UAS-Rab1.RNAi $^{TRiP.JF02609}$* (III) (BDSC_27299); *y v ; UAS-Rop.RNAi ^{THU0467}* (III) (THFC_THU0467); *y v ; UAS-Vps20.RNAi $^{VDRC.v47653}$/(TM3)* (VDRC_v47653); *w; UAS-VhaPPA1-1.RNAi $^{VDRC.v47188}$* (II) (VDRC_v47188); *w ; tub-GAL80^{ts} ; TM2/TM6B* (BDSC_7108); *w ; tub-GAL80^{ts}/TM2* (III) (BDSC_7017); *w , UAS-Dcr2 ; actin-GAL4/CyO* (THFC_TB00007); *y w ; EYFP-Rab4* (II) (BDSC_62542); *w ; EYFP-Rab5/CyO* (BDSC_62543); *w ; EYFP-Rab7* (III) (BDSC_62545); *w ; EYFP-Rab11* (III) (BDSC_62549); *w ; rn-GAL4/TM3, Sb, Ser* (BDSC_7405); *w ; UAS-3XFLAG-3xHA-Syx1-44-1* (III) (this study); *w ; UAS-3XFLAG-3xHA-Syx4-7-2* (III) (this study); *w ; UAS-3XFLAG-3xHA-Syx7-5-1* (III) (this study); *w ; UAS-3XFLAG-3xHA-Syx17-3-4* (III) (this study); *w ; YFP-Rab1* (III) (BDSC_62539); *w ; YFP-Rab2* (III) (BDSC_62540); *y w ; UAS-YFP-RabX3* (III) (BDSC_23276); *w ; YFP-Rab6/(CyO)* (BDSC_62544); *w ; YFP-Rab9* (II) (BDSC_62547); *w YFP-Rab10* (BDSC_62548).

Transgenic constructs

UAS-Rop-GFP

The coding sequence of Rop was amplified by PCR from whole L3 larva cDNA using primers attRop-F and attRop-R (see Table S2). This fragment was purified through gel extraction using HiPure Gel Pure DNA Mini Kit (cat# D2111-02; Magen) and cloned into vector pDONR221 (cat# 12536017; Thermo Fisher Scientific) with Gateway BP Clonase II Enzyme Mix (cat# 11789100; Invitrogen) to obtain entry clone pDONR221-Rop. From there, Rop was transferred to destination vector pTWG (UASt-Gateway cassette-GFP, stock# 1076; *Drosophila* Genomics Research Center [DGRC]) by Gateway LR recombination using Gateway LR Clonase II Enzyme Mix (cat# 11791100; Invitrogen).

UAS-Vps20-GFP

The coding sequence of Vps20 was amplified by PCR from whole L3 larva cDNA using primers attVps20-F and attVps20-R (see Table S2). This fragment was purified through gel extraction and cloned into pDONR221 to obtain pDONR221-Vps20. From there, Vps20 was transferred to destination vector pTWG (UASt-Gateway cassette-GFP, stock# 1076; DGRC) by Gateway LR recombination.

UAS-GFP-Syx17

The coding sequence of Syx17 was amplified by PCR from whole L3 larva cDNA using primers attSyx17-F and attSyx17-R (see Table S2). This fragment was purified through gel extraction and cloned into pDONR221 to obtain pDONR221-Syx17. From there, Syx17 was transferred to destination vector pTGW (UASt-GFP-Gateway cassette, stock# 1075; DGRC) by Gateway LR recombination.

UAS-mRFP-Rab1^{DN}

Rab1^{DN}, encoding dominant negative form of Rab1, was PCR amplified from whole L3 larva cDNA of fly strain BDSC 9757 (UAS-YFP-Rab1^{DN}). Primers adding att sites at the 5′ and 3′ termini of Rab1^{DN} were used: attRab1DN-F and attRab1DN-R (see Table S2). The resulting fragment was cloned into plasmid pDONR221 to obtain pDONR221-Rab1^{DN} and from there transferred to pTRW (UASt-mRFP-Gateway cassette, stock# 1135; DGRC) using Gateway LR recombination.

UAS-mRFP-Syx1, UAS-3xFLAG-3xHA-Syx1, UAS-mRFP-Syx4, UAS-3XFLAG-3xHA-Syx4, UAS-mRFP-Syx7 UAS-3XFLAG-3xHA-Syx7, UAS-mRFP-Syx17, and UAS-3XFLAG-3xHA-Syx17

The coding sequences of Syx1, Syx4, and Syx7 were amplified by PCR from whole L3 larva cDNA using primer pairs attSyx1-F and attSyx1-R, attSyx4-F and attSyx4-R, and attSyx7-F and attSyx7-R (see Table S2). The resulting fragments were purified through gel extraction and cloned into pDONR221 to obtain pDONR221-Syx1, pDONR221-Syx4, and pDONR221-Syx7. From there, Syx1, Syx4, Syx7, and Syx17 were transferred to destination vectors pTRW (UASt-mRFP-Gateway cassette, stock# 1135; DGRC) and pTFHW (UASt-3xFLAG-3xHA-Gateway cassette, stock# 1123; DGRC) by Gateway LR recombination.

Immunohistochemistry

For antibody staining of larval fat body (Figs. 2, B, C, E and I; 7 A; and Fig. S4 E), larvae were predissected in PBS by turning them inside out with fine-tip forceps, fixed in PBS containing 4% paraformaldehyde (cat# 80096692; Sinopharm Chemical Reagent; 20 min), washed in PBS (2 × 15 min), blocked in 0.1% PBT-BSA (PBS containing 0.1% Triton X-100 detergent [cat# T8787;

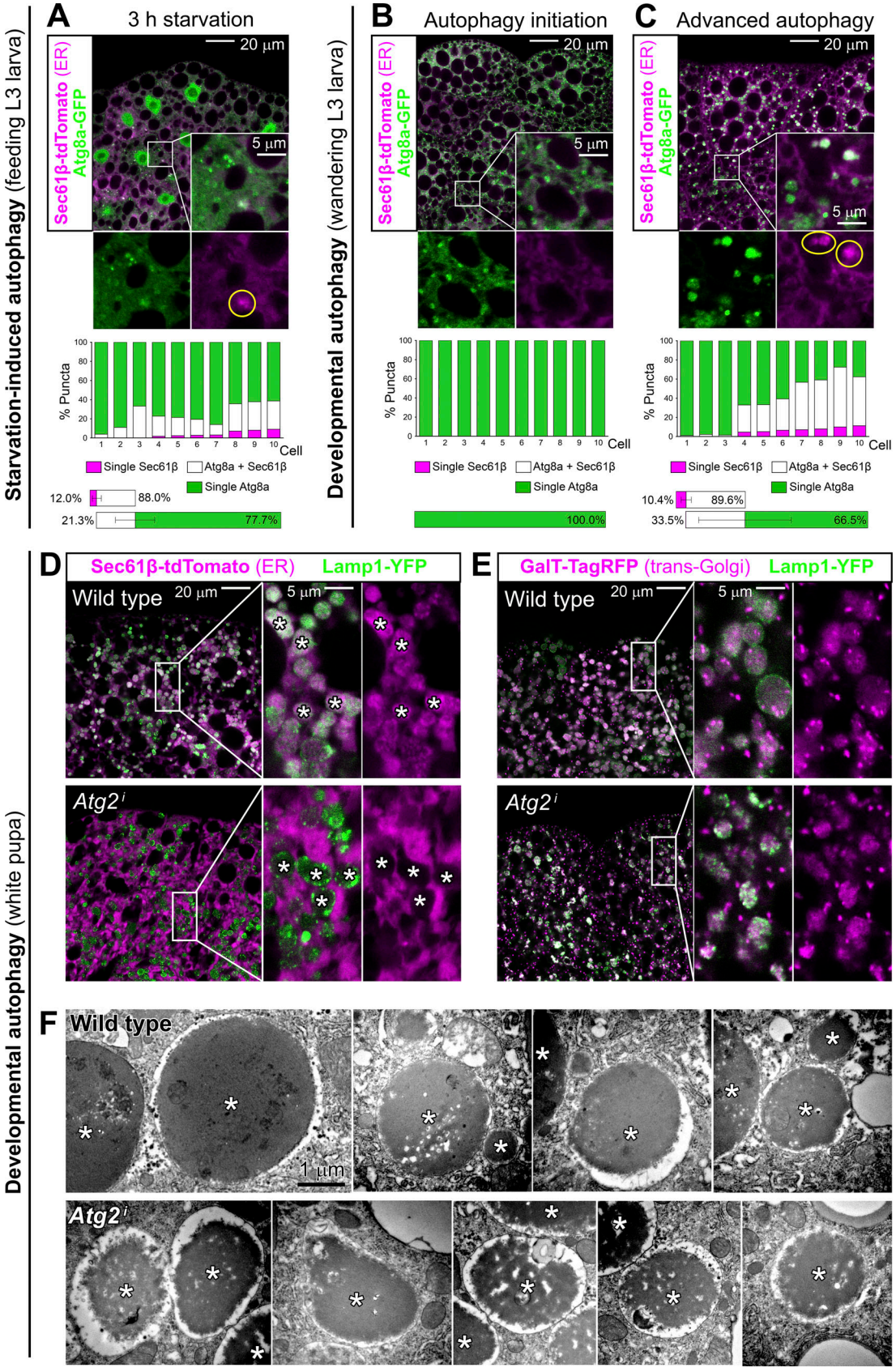

Figure 9. **Incorporation of ER marker Sec61β into autophagic vesicles is a late event that depends on Atg2. (A)** Confocal image of L3 fat body starved for 3 h showing autophagic marker Atg8a-GFP (green) and ER marker Sec61β-tdTomato (magenta), both driven by *BM-40-SPARC-GAL4*. Magnified inset in the lower right corner, with separate channels below. The graphs below quantify proximity between Atg8a-GFP puncta and Sec61β-tdTomato concentrations

(yellow circle) measured in 10 different cells, as well as average proximity values (n = 10, error bars indicate SD). **(B)** Atg8a-GFP (green) and Sec61β-tdTomato (magenta) in L3 fat body initiating programmed autophagy. No Sec61β concentrations are observed. **(C)** Atg8a-GFP (green) and Sec61β-tdTomato (magenta) in L3 fat body during advanced programmed autophagy. **(D)** Confocal images of Lamp1-YFP (green) and Sec61β-tdTomato (magenta) in fat body from wild-type (upper image) and *BM-40-SPARC>Atg2*^{i} (lower image) white pupae. Magnified insets show presence of Sec61β in autophagic vesicles in the wild type and complete absence upon Atg2 knockdown, with the Sec61β channel separated on the right (examples marked with asterisks). **(E)** Lamp1-YFP (green) and trans-Golgi GalT-TagRFP (magenta) in fat body from wild-type and *BM-40-SPARC>Atg2*^{i} white pupae. Magnified insets show presence of GalT in autophagic vesicles unaffected upon Atg2 knockdown, with the GalT channel separated on the right. **(F)** TEM micrographs of autophagic vesicles (autolysosomes, marked with asterisks) in fat body from wild-type (upper row) and *BM-40-SPARC>Atg2*^{i} (lower row) white pupae.

Sigma-Aldrich], 1% BSA [Cat# 201903A28; Zhongkekeao], and 250 mM NaCl [cat# 0805C384; Amresco]; 3 × 20 min), incubated overnight with primary antibody in PBT-BSA at 4°C, washed in PBT-BSA (3 × 20 min), incubated for 2 h with secondary antibody in PBT-BSA at RT, and then washed in PBT-BSA (3 × 20 min) and PBS (3 × 20 min). Tissues were finally dissected and mounted on a glass slide with a drop of DAPI-Vectashield (cat# H-1200; Vector Laboratories). Guinea pig anti-Tango1 (used at 1:1,000 dilution) was a gift from Sally Horne-Badovinac, University of Chicago, Chicago, IL (Lerner et al., 2013). Goat anti-Golgin245 (used at 1:1,000 dilution) was obtained from the Developmental Studies Hybridoma Bank (Riedel et al., 2016). Rabbit anti-Ref(2)P (used at 1:500 dilution) was purchased from Abcam (cat# 178440). Secondary antibodies used were: Rhodamine-conjugated goat anti-guinea pig IgG (1:200, cat# 106025003; Jackson ImmunoResearch); Alexa Fluor 647–conjugated goat anti-guinea pig IgG (1:200, cat# 106605003; Jackson ImmunoResearch), Alexa Fluor 488–conjugated donkey anti-rabbit IgG (1:200, cat# A21206; Invitrogen), and Alexa Flour 555–conjugated donkey anti-goat IgG H&L (1:500, cat# ab150130; Abcam).

F-actin phalloidin staining (Fig. S3 B) was performed with Alexa Fluor 647 phalloidin (1:25 of stock solution in DMSO, cat# A22287; Invitrogen) in PBT (PBS containing 0.1% Triton X-100) for 2 h.

For LysoTracker staining (Fig. S1 D), fat body from wandering or L3 larvae was dissected in Schneider's *Drosophila* medium (cat# 21720-024; GIBCO), and then incubated for 30 min in medium containing 71.43 nM LysoTracker Red (cat# C1046; Beyotime). Tissues were washed in medium (2 × 15 min) and mounted in PBS for immediate imaging on a glass slide with coverslip spacers to avoid crashing samples.

Fat body culture

Dissected L3 feeding larvae were incubated at RT in Schneider's *Drosophila* medium containing 2 µM Bafilomycin A (cat# ab120497; Abcam), 15 mg/ml chloroquine (cat# ab142116; Abcam), 0.25 mg/ml Cytochalasin D (cat# PHZ1063; Invitrogen), or 100 µg/ml BFA (cat# S1536; Beyotime). After culture of 6 h (Cytochalasin D and BFA) or 12 h (Bafilomycin A and chloroquine), samples were fixed in PBS containing 4% paraformaldehyde (20 min), washed in PBS (3 × 15 min), and mounted in DAPI-Vectashield.

Light imaging

Confocal microscopy images of fat body and other tissues were acquired at RT in a ZEISS LSM780 microscope equipped with Plan-Apochromat 63× oil (NA 1.4) and 100× oil (NA 1.4) objectives. Tissues were predissected in PBS by turning larvae inside out with fine tip forceps, fixed in PBS containing 4% paraformaldehyde (20 min), washed in PBS (3 × 15 min), and finally dissected and mounted on a glass slide with DAPI-Vectashield.

For SIM images (Fig. 3, A and B), 3D-SIM image stacks with a z-step of 0.24 µm were acquired at RT with a Nikon A1 N-SIM STORM microscope equipped with a CFI Apo SR TIRF 100× oil (NA 1.49) objective and an Andor Technology EMCCD camera (iXON DU-897 X-9255). Laser lines at 405, 488, and 561 were used for excitation. SIM image reconstructions were performed with NIS-Elements software (Nikon). Images are maximum intensity projections of three to five confocal sections.

Time-lapse images of blood cells in vivo (Fig. 4 and Video 2) were acquired at RT in an Andor Dragonfly inverted spinning-disc confocal microscopy system equipped with a 60× oil objective (NA 1.35, oil, Olympus UPlanSApo) and a Zyla 4.2 sCMOS camera. For animal imaging, L3 instar larvae were gently washed in water with a brush to remove food, dried on a paper napkin, and sandwiched between a glass slide and a mildly pressing coverslip held by four pieces of modeling clay on the corners. For each series, Z-stacks of 7-9 slices spaced 1 µm were acquired every 6 s for 10 min. Z stacks were processed with Fiji-ImageJ software (National Institutes of Health) using maximum intensity projection and bleach correction.

TEM

Larvae were predissected by turning them inside out in fixation solution containing 2.5% glutaraldehyde (cat# 18426; TED PELLA), 2% paraformaldehyde (cat# 43368; Alfa Aesar), and 0.1 M phosphate buffer (PB). 0.1 M PB was prepared with Na_2HPO_4 (cat# A11817; Alfa Aesar) and NaH_2PO_4 (cat# 0571-500G; Amresco), with pH 7.2. Prefixation was conducted at RT for 2 h in the same fixation solution. After this, predissected larvae were washed in 0.1 M PB (3 × 7 min, RT). Then, tissues were transferred to 0.1 M PB and post-fixed 30 min in a mixture of 1% osmic acid (cat# 018456; Tedpellco) and potassium hexacyanoferrate (cat# 60299-100G-F; Sigma-Aldrich) at RT avoiding light. Samples were then washed with MiliQ H_2O (5 × 7 min, RT), incubated with 1% uranyl acetate (cat# 8473; Merck) in the dark overnight at 4°C, washed with MiliQ H_2O (5 × 7 min, RT), and dehydrated in a series of 5-min washes on ice with prechilled 30, 50, 70, 90, and 100% (twice) ethanol (cat# 104021; Tongguang Jingxi Huagong), acetone/ethanol (1:1), and 100% acetone (cat# 105003; Tongguang Jingxi Huagong). Infiltration was conducted at RT with a mixture of acetone and resin 1:1 for 1.5 h, 1:2 for 3 h, and 1:3 overnight. The next day, samples were immersed in resin (3 × 3 h and then overnight, RT) consisting of 48% (vol/vol) SPI-PON 812 (Epoxy Resin Monomer, cat# 02659-AB, SPI-CHEM), 16% DDSA (Dodecenyl Succinic Anhydride, cat#

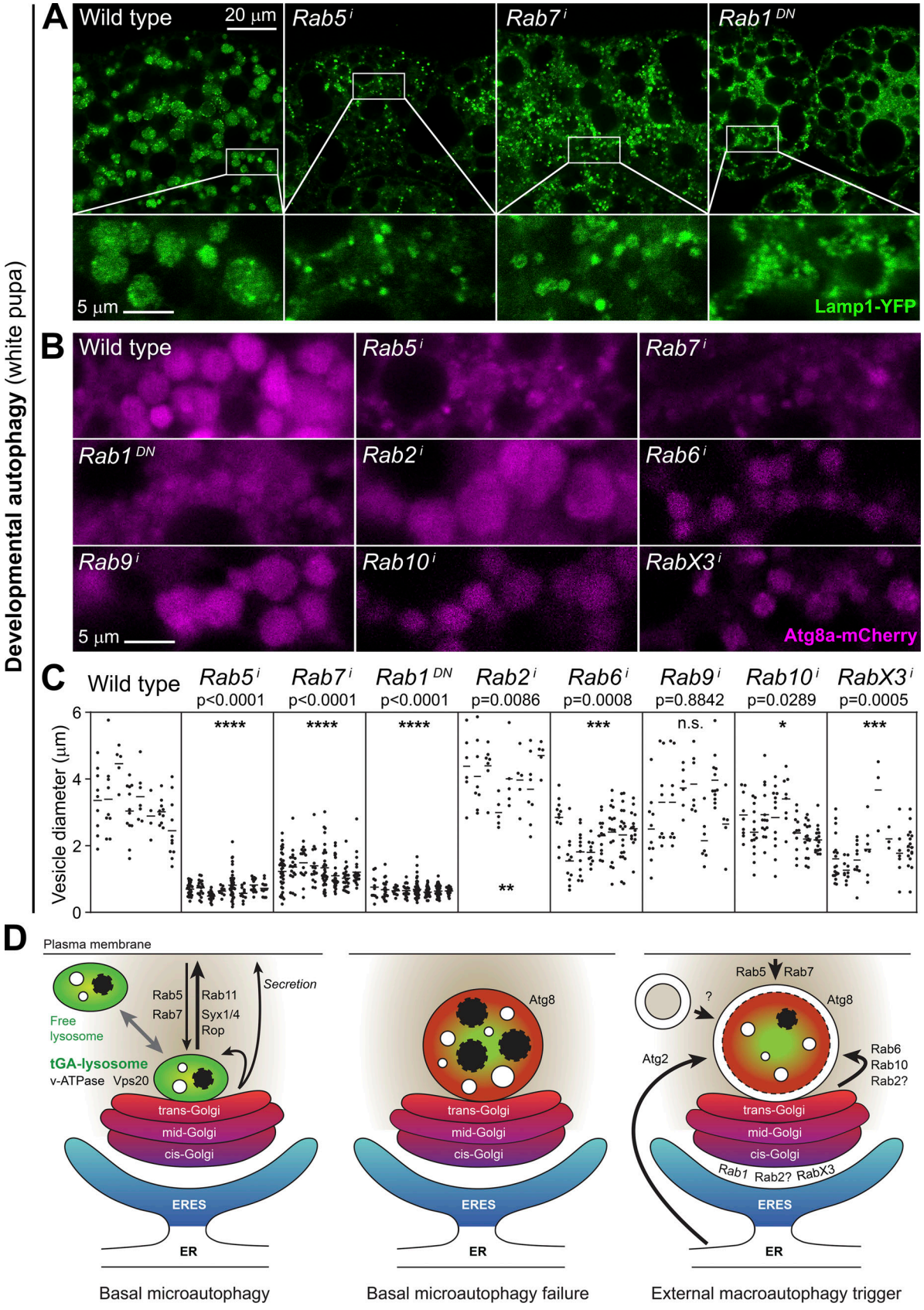

Figure 10. **Contributions of secretory and endosomal traffic to the growth of autophagic vesicles. (A)** Confocal images of fat body cells from wil- type, *BM-40-SPARC>Rab5*^{i}, *>Rab7*^{i}, and *>Rab1*^{DN} white pupae (0–1 h after puparium formation) showing lysosomal marker Lamp1-YFP (green). Magnified insets are shown below each image. **(B)** Autophagic vesicles marked with Atg8a-mCherry (magenta) in fat body from wild-type, *BM-40-SPARC>Rab5*^{i}, *>Rab7*^{i}, *>Rab1*^{DN},

>*Rab2*^{i}, >*Rab6*^{i}, >*Rab9*^{i}, >*Rab10*^{i}, and >*Rab9Fb(X3)*^{i} white pupae. **(C)** Autophagic vesicle diameter in wild-type, *BM-40-SPARC>Rab5*^{i}, >*Rab7*^{i}, >*Rab1*^{DN}, >*Rab2*^{i}, >*Rab6*^{i}, >*Rab9*^{i}, >*Rab10*^{i}, and >*Rab9Fb(X3)*^{i} white pupae. For each genotype, vesicle diameters (dots) inside eight square areas (21.255 × 21.255 µm) are represented. Horizontal lines indicate mean diameter in each area. P values from nested *t* tests of differences with the wild type are reported. n.s., P > 0.05; *, 0.05 > P > 0.01; **, 0.01 > P > 0.001; ***, 0.001 > P > 0.0001; and ****, P < 0.0001. **(D)** Model depicting the location and role of tGA-lysosomes. In normal conditions, basal microautophagy occurs in tGA-lysosomes, including degradation of excess or misrouted secretory cargo (crinophagy). Basal microautophagy failure or external macroautophagy induction results in formation of autophagic vesicles (autolysosomes) with contributions from endocytic and secretory routes, ER, and autophagosomes formed elsewhere.

02827-AF, SPI-CHEM), 34% NMA (Nadic Methyl Anhydride, cat# 02828-AF, SPI-CHEM), and 2% DMP-30 (2,4,6-Tris-dimethylaminomethyl phenol, cat# 02823-DA, SPI-CHEM). Tissues were then dissected from the carcasses and placed in block molds filled with resin for hardening at 60°C during 48 h. 70-nm ultrathin sections were cut from blocks on a Leica EM UC7 ultramicrotome and imaged in a Hitachi H-7650B electron microscope.

FIB-SEM

Sample preparation

FIB-SEM imaging was performed as previously described (Yang et al., 2021). Resin blocks containing tissues were obtained mostly as described above for TEM. Larvae were predissected and fixed in the fixation solution. After this, predissected larvae were washed in 0.1 M PB (3 × 7 min, RT). For APEX staining (one of two fat body samples), 30% H_2O_2 (cat# 10011218; Guoyao) was quickly mixed in DAB solution to a 0.03% (vol/vol) concentration during the wash. To prepare the DAB solution, DAB (3,3′-Diaminobenzidine, cat# D56637-1G; Sigma-Aldrich) was freshly dissolved in 0.1 M PB (pH 7.2) to a 0.5 mg/ml concentration and kept at 4°C avoiding light. The larvae were incubated in the H_2O_2/DAB mixture on a glass depression well at 4°C for 5–10 min, gently shaking in the dark. Both APEX-stained and unstained tissues were transferred to 0.1 M PB and post-fixed as for TEM. Post-fixation times were 30 min for fat body and 20 min for imaginal disc tissues. The following steps to get hardened blocks were the same as with TEM, except 2% BDMA (N,N-Dimethylbenzylamine, cat# 02821-CA, SPI-CHEM) rather than DMP-30 were used as epoxy accelerator when preparing resin.

Image acquisition

Resin blocks containing fat body or wing discs were trimmed to expose tissues, adhered to a 45/90° screw type holder (φ 12.7 mm * 22.8 mm, cat# ZB-Y1811; Zhongxingbairui), and coated with gold using a HITACHI E-1010 ion sputter coater for 120 s. FIB-SEM imaging was performed in a FEI Helios NanoLab G3 dual-beam microscope system equipped with Everhart-Thornley Detector, Through Lens Detector, and In Column Detector cameras. A 0.6 µm protective Pt coat was applied to the region of interest through gas injection prior to FIB milling and SEM imaging. For milling slices, an ion beam current of 0.43 nA at 30 kV acceleration voltage was used at a step of 20 nm. The parameters for SEM imaging were: 0.4 nA beam current, 2 kV acceleration voltage, 2 mm working distance, 8 µs dwell time, 4-nm pixel size, and 4,096 × 3,536 pixel count. TLD and ICD cameras collected backscattered signal for imaging. The imaging software was AutoSlice and View G3 1.7.2 (FEI).

Images acquired by FIB-SEM were imported into Dragonfly (Object Research Systems) and aligned through the SSD method in the Slide Registration panel. For segmentation, different regions of interest (ROIs) were created in the ROI tools panel. Each organelle was manually segmented as an individual ROI with the ROI Painter round brush tool in 2D mode. After segmentation in sections, ROIs were exported and saved as object files. Objects were then converted into 3D meshes using the export box in the ROI Tools panel to create meshes. Meshes were smoothed 4–6 times and observed in 3D scene mode. We used Movie Maker tools within Dragonfly to create movies of rotating Golgi for Video 1.

Image analysis

For quantification of marker association (apparent contact or overlap in confocal microsocopy images; Figs. 2, G, H, and L; 5, C and D; 6 D; 7 B; 8, C and D; 9, A–C; Figs. S2, A–C; and S3, B, C, and E), number of single and proximal puncta was manually counted using the point selection tool in ImageJ-FIJI. 10 cells per genotype from three to five different tissues were quantified, except for Fig. S2 A, where association was quantified in 10 square areas 300 × 300 pixel (12.454 × 12.454 µm) for central nervus system (CNS) and wing disc, and in 10 individual blood cells. For quantification of marker association throughout mitosis (Fig. S3 B), number of single and associated puncta was counted in 10, 14, 3, 6, and 1 cell for prophase, metaphase, anaphase, telophase, and cytokinesis, respectively, found in three different discs; interphase association was quantified in 10 square areas of 150 × 150 pixel (6.23 × 6.23 µm). For quantification of Rop-GFP recruitment to the plasma membrane (Fig. 5 F and Fig. S4 B), FIJI-ImageJ was used. GFP intensities were measured in 10 cells per genotype for plasma membrane ("brush selection" tool, with a 30 px width) and rest of the cell ("polygon selection" tool), and the ratio between them was calculated. For quantification of trans-Golgi and mid-Golgi sizes (Fig. 6 H and Fig. S4 F), the area of 100 puncta per genotype was measured using the "polygon selection" tool in FIJI-ImageJ-FIJI. For quantification of autophagic vesicle size (Fig. 10 C), vesicle diameter was manually measured with the line tool in ImageJ-FIJI. 8 different square areas 512 × 512 pixel (21.255 × 21.255 µm) were measured per genotype. For quantification of intracellular Collagen IV accumulation (Fig. S1 B), the area of 10 fat body adipocytes was delimited using the "polygon selection" tool in ImageJ-FIJI and Col IV α2-GFP intensity inside was measured inside. For quantification of LysoTracker staining (Fig. S1, E and F), the area of vesicles was delimited using the "oval selection" tool in ImageJ-FIJI.

Statistical analysis

Graphic representation and statistical analysis were performed using GraphPad Prism software. After data passed D'Agostino-Pearson normality tests, unpaired *t* tests (Figs. 5 F, 6 H, Fig. S1 B,

and Fig. S4 B) or nested *t* tests (Fig. 10 C) were conducted to test significance of differences with the wild type. P values are reported in graphs themselves or in figure legends. n.s., $P > 0.05$; *, $0.05 > P > 0.01$; **, $0.01 > P > 0.001$; ***, $0.001 > P > 0.0001$; and ****, $P < 0.0001$.

Online supplemental material

Fig. S1 shows confirmation and additional characterization of Rop, Vps20, and VhaPPA1-1 hits. Fig. S2 shows association with the trans-Golgi of Lamp1 in different tissues and of GAL4/UAS-expressed Rab-GTPases in fat body. Fig. S3 documents free lysosomes and multivesicular bodies through TEM, and quantifies tGA-lysosomes during mitosis and upon treatment with Cytocalasin D and BFA. Fig. S4 shows supporting evidence of interaction between Rop and Syx1/4. Fig. S5 documents Golgi localization of different Rab-GTPases. Video 1 shows animated 3D renderings of Golgi and tGA-lysosomes reconstructed from FIB-SEM data. Video 2 shows examples of lysosome association and dissociation behaviors with respect to the trans-Golgi. Table S1 lists experimental genotypes in the study. Table S2 lists primers used.

Acknowledgments

We thank Sally Horne-Badovinac, the Developmental Studies Hybridoma Bank, Bloomington *Drosophila* Stock Center, Kyoto Stock Center, Vienna *Drosophila* RNAi Center, Tsinghua Fly Center, and DGRC for providing antibodies, fly strains, and plasmids.

This work was supported by grants 91854207, 31771600, 31750410689, and 31701248 from the Natural Science Foundation of China, and grant PID2021-127112NB-I00 from Ministerio de Ciencia e Innovación, co-financed by the European Regional Development Fund. The Institute of Neurosciences is a "Severo Ochoa" Center of Excellence (SEV-2017-0723).

The authors declare no competing financial interests.

Author contributions: L. Zhou, X. Xue, K. Yang, Z. Feng, M. Liu, and J.C. Pastor-Pareja conducted research. L. Zhou, X. Xue, K. Yang, and J.C. Pastor-Pareja analyzed the data. L. Zhou, X. Xue, and J.C. Pastor-Pareja wrote the manuscript.

Submitted: 11 March 2022
Revised: 17 August 2022
Accepted: 23 September 2022

References

Ayala, C.I., J. Kim, and T.P. Neufeld. 2018. Rab6 promotes insulin receptor and cathepsin trafficking to regulate autophagy induction and activity in Drosophila. *J. Cell Sci.* 131:jcs216127. https://doi.org/10.1242/jcs.216127

Bannykh, S.I., T. Rowe, and W.E. Balch. 1996. The organization of endoplasmic reticulum export complexes. *J. Cell Biol.* 135:19–35. https://doi.org/10.1083/jcb.135.1.19

Bard, F., L. Casano, A. Mallabiabarrena, E. Wallace, K. Saito, H. Kitayama, G. Guizzunti, Y. Hu, F. Wendler, R. Dasgupta, et al. 2006. Functional genomics reveals genes involved in protein secretion and Golgi organization. *Nature*. 439:604–607. https://doi.org/10.1038/nature04377

Barlowe, C.K., and E.A. Miller. 2013. Secretory protein biogenesis and traffic in the early secretory pathway. *Genetics*. 193:383–410. https://doi.org/10.1534/genetics.112.142810

Bilder, D., K. Ong, T.-C. Hsi, K. Adiga, and J. Kim. 2021. Tumour–host interactions through the lens of Drosophila. *Nat. Rev. Cancer*. 21:687–700. https://doi.org/10.1038/s41568-021-00387-5

Brand, A.H., and N. Perrimon. 1993. Targeted gene expression as a means of altering cell fates and generating dominant phenotypes. *Development*. 118:401–415. https://doi.org/10.1242/dev.118.2.401

Brandizzi, F., and C. Barlowe. 2013. Organization of the ER-Golgi interface for membrane traffic control. *Nat. Rev. Mol. Cell Biol.* 14:382–392. https://doi.org/10.1038/nrm3588

Braulke, T., and J.S. Bonifacino. 2009. Sorting of lysosomal proteins. *Biochim. Biophys. Acta*. 1793:605–614. https://doi.org/10.1016/j.bbamcr.2008.10.016

Burgess, J., L.M. Del Bel, C.-I.J. Ma, B. Barylko, G. Polevoy, J. Rollins, J.P. Albanesi, H. Krämer, and J.A. Brill. 2012. Type II phosphatidylinositol 4-kinase regulates trafficking of secretory granule proteins in Drosophila. *Development*. 139:3040–3050. https://doi.org/10.1242/dev.077644

Chen, W., Y. Feng, D. Chen, and A. Wandinger-Ness. 1998. Rab11 is required for trans-Golgi network–to–plasma membrane transport and a preferential target for GDP dissociation inhibitor. *Mol. Biol. Cell*. 9:3241–3257. https://doi.org/10.1091/mbc.9.11.3241

Chowdhury, S., C. Otomo, A. Leitner, K. Ohashi, R. Aebersold, G.C. Lander, and T. Otomo. 2018. Insights into autophagosome biogenesis from structural and biochemical analyses of the ATG2A-WIPI4 complex. *Proc. Natl. Acad. Sci. USA*. 115:E9792–E9801. https://doi.org/10.1073/pnas.1811874115

Csizmadia, T., P. Lorincz, K. Hegedus, S. Szeplaki, P. Low, and G. Juhasz. 2018. Molecular mechanisms of developmentally programmed crinophagy in Drosophila. *J. Cell Biol.* 217:361–374. https://doi.org/10.1083/jcb.201702145

Cui, Y., S. Parashar, M. Zahoor, P.G. Needham, M. Mari, M. Zhu, S. Chen, H.C. Ho, F. Reggiori, H. Farhan, et al. 2019. A COPII subunit acts with an autophagy receptor to target endoplasmic reticulum for degradation. *Science*. 365:53–60. https://doi.org/10.1126/science.aau9263

Dai, J., M. Ma, Z. Feng, and J.C. Pastor-Pareja. 2017. Inter-adipocyte adhesion and signaling by collagen IV intercellular concentrations in Drosophila. *Curr. Biol.* 27:2729–2740.e4. https://doi.org/10.1016/j.cub.2017.08.002

Day, K.J., J.C. Casler, and B.S. Glick. 2018. Budding yeast has a minimal endomembrane system. *Dev. Cell*. 44:56–72.e4. https://doi.org/10.1016/j.devcel.2017.12.014

De Matteis, M.A., and A. Luini. 2008. Exiting the Golgi complex. *Nat. Rev. Mol. Cell Biol.* 9:273–284. https://doi.org/10.1038/nrm2378

De Tito, S., J.H. Hervás, A.R. van Vliet, and S.A. Tooze. 2020. The Golgi as an assembly line to the autophagosome. *Trends Biochem. Sci.* 45:484–496. https://doi.org/10.1016/j.tibs.2020.03.010

Deng, S., J. Liu, X. Wu, and W. Lu. 2020. Golgi apparatus: A potential therapeutic target for autophagy-associated neurological diseases. *Front. Cell Dev. Biol.* 8:564975. https://doi.org/10.3389/fcell.2020.564975

DeVorkin, L., and S.M. Gorski. 2014. Monitoring autophagic flux using Ref(2)P, the Drosophila p62 ortholog. *Cold Spring Harb. Protoc.* 2014:959–966. https://doi.org/10.1101/pdb.prot080333

Dunst, S., T. Kazimiers, F. von Zadow, H. Jambor, A. Sagner, B. Brankatschk, A. Mahmoud, S. Spannl, P. Tomancak, S. Eaton, and M. Brankatschk. 2015. Endogenously tagged rab proteins: A resource to study membrane trafficking in Drosophila. *Dev. Cell*. 33:351–365. https://doi.org/10.1016/j.devcel.2015.03.022

Farhan, H., M. Kundu, and S. Ferro-Novick. 2017. The link between autophagy and secretion: A story of multitasking proteins. *Mol. Biol. Cell*. 28:1161–1164. https://doi.org/10.1091/mbc.E16-11-0762

Farkas, R., D. Benova-Liszekova, L. Mentelova, S. Mahmood, Z. Datkova, M. Beno, L. Pecenova, O. Raska, J. Smigova, B.A. Chase, et al. 2015. Vacuole dynamics in the salivary glands of Drosophila melanogaster during prepupal development. *Dev. Growth Differ.* 57:74–96. https://doi.org/10.1111/dgd.12193

Feng, Z., K. Yang, and J.C. Pastor-Pareja. 2020. Tales of the ER-Golgi frontier: Drosophila-centric considerations on Tango1 function. *Front. Cell Dev. Biol.* 8:619022. https://doi.org/10.3389/fcell.2020.619022

Fölsch, H., H. Ohno, J.S. Bonifacino, and I. Mellman. 1999. A novel clathrin adaptor complex mediates basolateral targeting in polarized epithelial cells. *Cell*. 99:189–198. https://doi.org/10.1016/s0092-8674(00)81650-5

Fujii, S., K. Kurokawa, R. Inaba, N. Hiramatsu, T. Tago, Y. Nakamura, A. Nakano, T. Satoh, and A.K. Satoh. 2020a. Recycling endosomes attach to the trans-side of Golgi stacks in Drosophila and mammalian cells. *J. Cell Sci.* 133:jcs236935. https://doi.org/10.1242/jcs.236935

Fujii, S., T. Tago, N. Sakamoto, T. Yamamoto, T. Satoh, and A.K. Satoh. 2020b. Recycling endosomes associate with Golgi stacks in sea urchin embryos. *Commun. Integr. Biol.* 13:59–62. https://doi.org/10.1080/19420889.2020.1761069

Fujita, N., W. Huang, T.H. Lin, J.F. Groulx, S. Jean, J. Nguyen, Y. Kuchitsu, I. Koyama-Honda, N. Mizushima, M. Fukuda, and A.A. Kiger. 2017.

Genetic screen in Drosophila muscle identifies autophagy-mediated T-tubule remodeling and a Rab2 role in autophagy. *Elife*. 6:e23367. https://doi.org/10.7554/eLife.23367

Galluzzi, L., E.H. Baehrecke, A. Ballabio, P. Boya, J.M. Bravo-San Pedro, F. Cecconi, A.M. Choi, C.T. Chu, P. Codogno, M.I. Colombo, et al. 2017. Molecular definitions of autophagy and related processes. *EMBO J.* 36: 1811–1836. https://doi.org/10.15252/embj.201796697

Ge, L., D. Melville, M. Zhang, and R. Schekman. 2013. The ER–Golgi intermediate compartment is a key membrane source for the LC3 lipidation step of autophagosome biogenesis. *Elife*. 2:e00947. https://doi.org/10.7554/eLife.00947

Gotz, T.W.B., D. Puchkov, V. Lysiuk, J. Lutzkendorf, A.G. Nikonenko, C. Quentin, M. Lehmann, S.J. Sigrist, and A.G. Petzoldt. 2021. Rab2 regulates presynaptic precursor vesicle biogenesis at the trans-Golgi. *J. Cell Biol.* 220:e202006040. https://doi.org/10.1083/jcb.202006040

Graef, M., J.R. Friedman, C. Graham, M. Babu, and J. Nunnari. 2013. ER exit sites are physical and functional core autophagosome biogenesis components. *Mol. Biol. Cell*. 24:2918–2931. https://doi.org/10.1091/mbc.E13-07-0381

Hegedűs, K., S. Takáts, A. Boda, A. Jipa, P. Nagy, K. Varga, A.L. Kovács, and G. Juhász. 2016. The Ccz1-Mon1-Rab7 module and Rab5 control distinct steps of autophagy. *Mol. Biol. Cell*. 27:3132–3142. https://doi.org/10.1091/mbc.E16-03-0205

Hennig, K.M., J. Colombani, and T.P. Neufeld. 2006. TOR coordinates bulk and targeted endocytosis in the Drosophila melanogaster fat body to regulate cell growth. *J. Cell Biol.* 173:963–974. https://doi.org/10.1083/jcb.200511140

Hu, S., Y. Li, and J. Shen. 2020. A diverse membrane interaction network for plant multivesicular bodies: Roles in proteins vacuolar delivery and unconventional secretion. *Front. Plant Sci.* 11:425. https://doi.org/10.3389/fpls.2020.00425

Huotari, J., and A. Helenius. 2011. Endosome maturation. *EMBO J.* 30: 3481–3500. https://doi.org/10.1038/emboj.2011.286

Itakura, E., C. Kishi-Itakura, and N. Mizushima. 2012. The hairpin-type tail-anchored SNARE syntaxin 17 targets to autophagosomes for fusion with endosomes/lysosomes. *Cell*. 151:1256–1269. https://doi.org/10.1016/j.cell.2012.11.001

Jacomin, A.C., M.O. Fauvarque, and E. Taillebourg. 2016. A functional endosomal pathway is necessary for lysosome biogenesis in Drosophila. *BMC Cell Biol.* 17:36. https://doi.org/10.1186/s12860-016-0115-7

Jacomin, A.C., R. Gohel, Z. Hussain, A. Varga, T. Maruzs, M. Eddison, M. Sica, A. Jain, K.G. Moffat, T. Johansen, et al. 2021. Degradation of arouser by endosomal microautophagy is essential for adaptation to starvation in Drosophila. *Life Sci. Alliance*. 4:e202000965. https://doi.org/10.26508/lsa.202000965

Jones, S.M., K.E. Howell, J.R. Henley, H. Cao, and M.A. McNiven. 1998. Role of dynamin in the formation of transport vesicles from the trans-Golgi network. *Science*. 279:573–577. https://doi.org/10.1126/science.279.5350.573

Jouandin, P., Z. Marelja, Y.H. Shih, A.A. Parkhitko, M. Dambowsky, J.M. Asara, I. Nemazanyy, C.C. Dibble, M. Simons, and N. Perrimon. 2022. Lysosomal cystine mobilization shapes the response of TORC1 and tissue growth to fasting. *Science*. 375:eabc4203. https://doi.org/10.1126/science.abc4203

Katheder, N.S., R. Khezri, F. O'Farrell, S.W. Schultz, A. Jain, M.M. Rahman, K.O. Schink, T.A. Theodossiou, T. Johansen, G. Juhasz, et al. 2017. Microenvironmental autophagy promotes tumour growth. *Nature*. 541: 417–420. https://doi.org/10.1038/nature20815

Ke, H., Z. Feng, M. Liu, T. Sun, J. Dai, M. Ma, L.P. Liu, J.Q. Ni, and J.C. Pastor-Pareja. 2018. Collagen secretion screening in Drosophila supports a common secretory machinery and multiple Rab requirements. *J. Genet. Genom.* 45:299–313. https://doi.org/10.1016/j.jgg.2018.05.002

Kim, S., S.A. Naylor, and A. DiAntonio. 2012. Drosophila Golgi membrane protein Ema promotes autophagosomal growth and function. *Proc. Natl. Acad. Sci. USA*. 109:E1072–E1081. https://doi.org/10.1073/pnas.1120320109

Kloepper, T.H., C.N. Kienle, and D. Fasshauer. 2008. SNAREing the basis of multicellularity: Consequences of protein family expansion during evolution. *Mol. Biol. Evol.* 25:2055–2068. https://doi.org/10.1093/molbev/msn151

Klumperman, J. 2011. Architecture of the mammalian Golgi. *Cold Spring Harbor Perspect. Biol.* 3:a005181. https://doi.org/10.1101/cshperspect.a005181

Klumperman, J., and G. Raposo. 2014. The complex ultrastructure of the endolysosomal system. *Cold Spring Harbor Perspect. Biol.* 6:a016857. https://doi.org/10.1101/cshperspect.a016857

Kondylis, V., H.E. van Nispen tot Pannerden, B. Herpers, F. Friggi-Grelin, and C. Rabouille. 2007. The golgi comprises a paired stack that is separated at G2 by modulation of the actin cytoskeleton through Abi and Scar/WAVE. *Dev. Cell*. 12:901–915. https://doi.org/10.1016/j.devcel.2007.03.008

Kondylis, V., and C. Rabouille. 2009. The Golgi apparatus: Lessons from Drosophila. *FEBS Lett.* 583:3827–3838. https://doi.org/10.1016/j.febslet.2009.09.048

Kotani, T., H. Kirisako, M. Koizumi, Y. Ohsumi, and H. Nakatogawa. 2018. The Atg2-Atg18 complex tethers pre-autophagosomal membranes to the endoplasmic reticulum for autophagosome formation. *Proc. Natl. Acad. Sci. USA*. 115:10363–10368. https://doi.org/10.1073/pnas.1806727115

Kreitzer, G., A. Marmorstein, P. Okamoto, R. Vallee, and E. Rodriguez-Boulan. 2000. Kinesin and dynamin are required for post-Golgi transport of a plasma-membrane protein. *Nat. Cell Biol.* 2:125–127. https://doi.org/10.1038/35000081

Lee, C.Y., and E.H. Baehrecke. 2001. Steroid regulation of autophagic programmed cell death during development. *Development*. 128:1443–1455. https://doi.org/10.1242/dev.128.8.1443

Lerner, D.W., D. McCoy, A.J. Isabella, A.P. Mahowald, G.F. Gerlach, T.A. Chaudhry, and S. Horne-Badovinac. 2013. A Rab10-dependent mechanism for polarized basement membrane secretion during organ morphogenesis. *Dev. Cell*. 24:159–168. https://doi.org/10.1016/j.devcel.2012.12.005

Lim, C.Y., and R. Zoncu. 2016. The lysosome as a command-and-control center for cellular metabolism. *J. Cell Biol.* 214:653–664. https://doi.org/10.1083/jcb.201607005

Lőrincz, P., S. Tóth, P. Benkő, Z. Lakatos, A. Boda, G. Glatz, M. Zobel, S. Bisi, K. Hegedűs, S. Takáts, et al. 2017. Rab2 promotes autophagic and endocytic lysosomal degradation. *J. Cell Biol.* 216:1937–1947. https://doi.org/10.1083/jcb.201611027

Lund, V.K., K.L. Madsen, and O. Kjaerulff. 2018. Drosophila Rab2 controls endosome-lysosome fusion and LAMP delivery to late endosomes. *Autophagy*. 14:1520–1542. https://doi.org/10.1080/15548627.2018.1458170

Luo, Y., S. Scholl, A. Doering, Y. Zhang, N.G. Irani, S.D. Rubbo, L. Neumetzler, P. Krishnamoorthy, I. Van Houtte, E. Mylle, et al. 2015. V-ATPase activity in the TGN/EE is required for exocytosis and recycling in Arabidopsis. *Nat. Plants*. 1:15094. https://doi.org/10.1038/nplants.2015.94

Luzio, J.P., Y. Hackmann, N.M. Dieckmann, and G.M. Griffiths. 2014. The biogenesis of lysosomes and lysosome-related organelles. *Cold Spring Harbor Perspect. Biol.* 6:a016840. https://doi.org/10.1101/cshperspect.a016840

Ma, C.-I.J., and J.A. Brill. 2021. Endosomal Rab GTPases regulate secretory granule maturation in Drosophila larval salivary glands. *Commun. Integr. Biol.* 14:15–20. https://doi.org/10.1080/19420889.2021.1874663

Ma, C.J., Y. Yang, T. Kim, C.H. Chen, G. Polevoy, M. Vissa, J. Burgess, and J.A. Brill. 2020. An early endosome-derived retrograde trafficking pathway promotes secretory granule maturation. *J. Cell Biol.* 219:e201808017. https://doi.org/10.1083/jcb.201808017

Maruzs, T., P. Lőrincz, Z. Szatmári, S. Széplaki, Z. Sándor, Z. Lakatos, G. Puska, G. Juhász, and M. Sass. 2015. Retromer ensures the degradation of autophagic cargo by maintaining lysosome function in Drosophila. *Traffic*. 16:1088–1107. https://doi.org/10.1111/tra.12309

Maruzs, T., Z. Simon-Vecsei, V. Kiss, T. Csizmadia, and G. Juhasz. 2019. On the fly: Recent progress on autophagy and aging in Drosophila. *Front. Cell Dev. Biol.* 7:140. https://doi.org/10.3389/fcell.2019.00140

Mauvezin, C., C. Ayala, C.R. Braden, J. Kim, and T.P. Neufeld. 2014. Assays to monitor autophagy in Drosophila. *Methods*. 68:134–139. https://doi.org/10.1016/j.ymeth.2014.03.014

Mauvezin, C., P. Nagy, G. Juhasz, and T.P. Neufeld. 2015. Autophagosome-lysosome fusion is independent of V-ATPase-mediated acidification. *Nat. Commun.* 6:7007. https://doi.org/10.1038/ncomms8007

McGuire, S.E., P.T. Le, A.J. Osborn, K. Matsumoto, and R.L. Davis. 2003. Spatiotemporal rescue of memory dysfunction in Drosophila. *Science*. 302:1765–1768. https://doi.org/10.1126/science.1089035

Mesquita, A., J. Glenn, and A. Jenny. 2021. Differential activation of eMI by distinct forms of cellular stress. *Autophagy*. 17:1828–1840. https://doi.org/10.1080/15548627.2020.1783833

Mukherjee, A., B. Patel, H. Koga, A.M. Cuervo, and A. Jenny. 2016. Selective endosomal microautophagy is starvation-inducible in Drosophila. *Autophagy*. 12:1984–1999. https://doi.org/10.1080/15548627.2016.1208887

Mulakkal, N.C., P. Nagy, S. Takats, R. Tusco, G. Juhasz, and I.P. Nezis. 2014. Autophagy in Drosophila: From historical studies to current knowledge. *Biomed. Res. Int.* 2014:273473. https://doi.org/10.1155/2014/273473

Nagano, M., J.Y. Toshima, D.E. Siekhaus, and J. Toshima. 2019. Rab5-mediated endosome formation is regulated at the trans-Golgi network. *Commun. Biol.* 2:419. https://doi.org/10.1038/s42003-019-0670-5

Neuman, S.D., A.R. Lee, J.E. Selegue, A.T. Cavanagh, and A. Bashirullah. 2021a. A novel function for Rab1 and Rab11 during secretory granule maturation. *J. Cell Sci.* 134:jcs259037. https://doi.org/10.1242/jcs.259037

Neuman, S.D., E.L. Terry, J.E. Selegue, A.T. Cavanagh, and A. Bashirullah. 2021b. Mistargeting of secretory cargo in retromer-deficient cells. *Dis. Model Mech.* 14:dmm046417. https://doi.org/10.1242/dmm.046417

Novick, P., C. Field, and R. Schekman. 1980. Identification of 23 complementation groups required for post-translational events in the yeast secretory pathway. *Cell*. 21:205–215. https://doi.org/10.1016/0092-8674(80)90128-2

Novikoff, A.B., and P.M. Novikoff. 1977. Cytochemical contributions to differentiating GERL from the Golgi apparatus. *Histochem. J.* 9:525–551. https://doi.org/10.1007/BF01002901

Ohashi, Y., and S. Munro. 2010. Membrane delivery to the yeast autophagosome from the Golgi-endosomal system. *Mol. Biol. Cell*. 21:3998–4008. https://doi.org/10.1091/mbc.E10-05-0457

Oku, M., Y. Maeda, Y. Kagohashi, T. Kondo, M. Yamada, T. Fujimoto, and Y. Sakai. 2017. Evidence for ESCRT- and clathrin-dependent microautophagy. *J. Cell Biol.* 216:3263–3274. https://doi.org/10.1083/jcb.201611029

Omari, S., E. Makareeva, A. Roberts-Pilgrim, L. Mirigian, M. Jarnik, C. Ott, J. Lippincott-Schwartz, and S. Leikin. 2018. Noncanonical autophagy at ER exit sites regulates procollagen turnover. *Proc. Natl. Acad. Sci. USA*. 115:E10099–E10108. https://doi.org/10.1073/pnas.1814552115

Pastor-Pareja, J.C. 2020. Atypical basement membranes and basement membrane diversity - what is normal anyway? *J. Cell Sci.* 133:jcs241794. https://doi.org/10.1242/jcs.241794

Pastor-Pareja, J.C., and T. Xu. 2011. Shaping cells and organs in Drosophila by opposing roles of fat body-secreted Collagen IV and perlecan. *Dev. Cell*. 21:245–256. https://doi.org/10.1016/j.devcel.2011.06.026

Pfeiffer, S., S. Ricardo, J.-B. Manneville, C. Alexandre, and J.-P. Vincent. 2002. Producing cells retain and recycle wingless in Drosophila embryos. *Curr. Biol.* 12:957–962. https://doi.org/10.1016/s0960-9822(02)00867-9

Pircs, K., P. Nagy, A. Varga, Z. Venkei, B. Erdi, K. Hegedus, and G. Juhasz. 2012. Advantages and limitations of different p62-based assays for estimating autophagic activity in Drosophila. *PLoS One*. 7:e44214. https://doi.org/10.1371/journal.pone.0044214

Pu, J., C.M. Guardia, T. Keren-Kaplan, and J.S. Bonifacino. 2016. Mechanisms and functions of lysosome positioning. *J. Cell Sci.* 129:4329–4339. https://doi.org/10.1242/jcs.196287

Rabouille, C. 2019. COPII vesicles and the expansion of the phagophore. *Elife*. 8:e44944. https://doi.org/10.7554/eLife.44944

Rahman, A., P. Lőrincz, R. Gohel, A. Nagy, G. Csordás, Y. Zhang, G. Juhász, and I.P. Nezis. 2022. GMAP is an Atg8a-interacting protein that regulates Golgi turnover in Drosophila. *Cell Rep.* 39:110903. https://doi.org/10.1016/j.celrep.2022.110903

Riedel, F., A.K. Gillingham, C. Rosa-Ferreira, A. Galindo, and S. Munro. 2016. An antibody toolkit for the study of membrane traffic in Drosophila melanogaster. *Biol. Open*. 5:987–992. https://doi.org/10.1242/bio.018937

Ripoche, J., B. Link, J.K. Yucel, K. Tokuyasu, and V. Malhotra. 1994. Location of Golgi membranes with reference to dividing nuclei in syncytial Drosophila embryos. *Proc. Natl. Acad. Sci. USA*. 91:1878–1882. https://doi.org/10.1073/pnas.91.5.1878

Robinson, D.G. 2020. Plant Golgi ultrastructure. *J. Microsc.* 280:111–121. https://doi.org/10.1111/jmi.12899

Roote, J., and A. Prokop. 2013. How to design a genetic mating scheme: A basic training package for Drosophila genetics. *G3*. 3:353–358. https://doi.org/10.1534/g3.112.004820

Rubin, G.M., and A.C. Spradling. 1982. Genetic transformation of Drosophila with transposable element vectors. *Science*. 218:348–353. https://doi.org/10.1126/science.6289436

Rusten, T.E., K. Lindmo, G. Juhasz, M. Sass, P.O. Seglen, A. Brech, and H. Stenmark. 2004. Programmed autophagy in the Drosophila fat body is induced by ecdysone through regulation of the PI3K pathway. *Dev. Cell*. 7:179–192. https://doi.org/10.1016/j.devcel.2004.07.005

Rusten, T.E., T. Vaccari, K. Lindmo, L.M.W. Rodahl, I.P. Nezis, C. Sem-Jacobsen, F. Wendler, J.-P. Vincent, A. Brech, D. Bilder, and H. Stenmark. 2007. ESCRTs and Fab1 regulate distinct steps of autophagy. *Curr. Biol.* 17:1817–1825. https://doi.org/10.1016/j.cub.2007.09.032

Scott, R.C., O. Schuldiner, and T.P. Neufeld. 2004. Role and regulation of starvation-induced autophagy in the Drosophila fat body. *Dev. Cell*. 7:167–178. https://doi.org/10.1016/j.devcel.2004.07.009

Shimizu, Y., J. Takagi, E. Ito, Y. Ito, K. Ebine, Y. Komatsu, Y. Goto, M. Sato, K. Toyooka, T. Ueda, et al. 2021. Cargo sorting zones in the trans-Golgi network visualized by super-resolution confocal live imaging microscopy in plants. *Nat. Commun.* 12:1901. https://doi.org/10.1038/s41467-021-22267-0

Simonsen, A., R.C. Cumming, A. Brech, P. Isakson, D.R. Schubert, and K.D. Finley. 2008. Promoting basal levels of autophagy in the nervous system enhances longevity and oxidant resistance in adult Drosophila. *Autophagy*. 4:176–184. https://doi.org/10.4161/auto.5269

Takats, S., P. Nagy, A. Varga, K. Pircs, M. Karpati, K. Varga, A.L. Kovacs, K. Hegedus, and G. Juhasz. 2013. Autophagosomal Syntaxin17-dependent lysosomal degradation maintains neuronal function in Drosophila. *J. Cell Biol.* 201:531–539. https://doi.org/10.1083/jcb.201211160

Tooze, S.A., A. Abada, and Z. Elazar. 2014. Endocytosis and autophagy: Exploitation or cooperation? *Cold Spring Harbor Perspect. Biol.* 6:a018358. https://doi.org/10.1101/cshperspect.a018358

Vaccari, T., T.E. Rusten, L. Menut, I.P. Nezis, A. Brech, H. Stenmark, and D. Bilder. 2009. Comparative analysis of ESCRT-I, ESCRT-II and ESCRT-III function in Drosophila by efficient isolation of ESCRT mutants. *J. Cell Sci.* 122:2413–2423. https://doi.org/10.1242/jcs.046391

Valverde, D.P., S. Yu, V. Boggavarapu, N. Kumar, J.A. Lees, T. Walz, K.M. Reinisch, and T.J. Melia. 2019. ATG2 transports lipids to promote autophagosome biogenesis. *J. Cell Biol.* 218:1787–1798. https://doi.org/10.1083/jcb.201811139

van Meel, E., and J. Klumperman. 2008. Imaging and imagination: Understanding the endo-lysosomal system. *Histochem. Cell Biol.* 129:253–266. https://doi.org/10.1007/s00418-008-0384-0

Vietri, M., M. Radulovic, and H. Stenmark. 2020. The many functions of ESCRTs. *Nat. Rev. Mol. Cell Biol.* 21:25–42. https://doi.org/10.1038/s41580-019-0177-4

Viotti, C., J. Bubeck, Y.D. Stierhof, M. Krebs, M. Langhans, W. van den Berg, W. van Dongen, S. Richter, N. Geldner, J. Takano, et al. 2010. Endocytic and secretory traffic in Arabidopsis merge in the trans-Golgi network/early endosome, an independent and highly dynamic organelle. *Plant Cell*. 22:1344–1357. https://doi.org/10.1105/tpc.109.072637

Wang, J., S. Davis, M. Zhu, E.A. Miller, and S. Ferro-Novick. 2017. Autophagosome formation: Where the secretory and autophagy pathways meet. *Autophagy*. 13:973–974. https://doi.org/10.1080/15548627.2017.1287657

Wang, J., S. Menon, A. Yamasaki, H.T. Chou, T. Walz, Y. Jiang, and S. Ferro-Novick. 2013. Ypt1 recruits the Atg1 kinase to the preautophagosomal structure. *Proc. Natl. Acad. Sci. USA*. 110:9800–9805. https://doi.org/10.1073/pnas.1302337110

Wendler, F., A.K. Gillingham, R. Sinka, C. Rosa-Ferreira, D.E. Gordon, X. Franch-Marro, A.A. Peden, J.P. Vincent, and S. Munro. 2010. A genome-wide RNA interference screen identifies two novel components of the metazoan secretory pathway. *EMBO J.* 29:304–314. https://doi.org/10.1038/emboj.2009.350

Wu, M.N., J.T. Littleton, M.A. Bhat, A. Prokop, and H.J. Bellen. 1998. ROP, the Drosophila Sec1 homolog, interacts with syntaxin and regulates neurotransmitter release in a dosage-dependent manner. *EMBO J.* 17:127–139. https://doi.org/10.1093/emboj/17.1.127

Wucherpfennig, T., M. Wilsch-Bräuninger, and M. González-Gaitán. 2003. Role of Drosophila Rab5 during endosomal trafficking at the synapse and evoked neurotransmitter release. *J. Cell Biol.* 161:609–624. https://doi.org/10.1083/jcb.200211087

Xu, H., and D. Ren. 2015. Lysosomal physiology. *Annu. Rev. Physiol.* 77:57–80. https://doi.org/10.1146/annurev-physiol-021014-071649

Yang, K., M. Liu, Z. Feng, M. Rojas, L. Zhou, H. Ke, and J.C. Pastor-Pareja. 2021. ER exit sites in Drosophila display abundant ER-Golgi vesicles and pearled tubes but no megacarriers. *Cell Rep.* 36:109707. https://doi.org/10.1016/j.celrep.2021.109707

Yim, W.W., and N. Mizushima. 2020. Lysosome biology in autophagy. *Cell Discov.* 6:6. https://doi.org/10.1038/s41421-020-0141-7

Young, A.R., E.Y. Chan, X.W. Hu, R. Köchl, S.G. Crawshaw, S. High, D.W. Hailey, J. Lippincott-Schwartz, and S.A. Tooze. 2006. Starvation and ULK1-dependent cycling of mammalian Atg9 between the TGN and endosomes. *J. Cell Sci.* 119:3888–3900. https://doi.org/10.1242/jcs.03172

Zang, Y., M. Wan, M. Liu, H. Ke, S. Ma, L.P. Liu, J.Q. Ni, and J.C. Pastor-Pareja. 2015. Plasma membrane overgrowth causes fibrotic collagen accumulation and immune activation in Drosophila adipocytes. *Elife*. 4:e07187. https://doi.org/10.7554/eLife.07187

Zhang, H., and E.H. Baehrecke. 2015. Eaten alive: Novel insights into autophagy from multicellular model systems. *Trends Cell Biol.* 25:376–387. https://doi.org/10.1016/j.tcb.2015.03.001

Zhu, L., J.R. Jorgensen, M. Li, Y.-S. Chuang, and S.D. Emr. 2017. ESCRTs function directly on the lysosome membrane to downregulate ubiquitinated lysosomal membrane proteins. *Elife*. 6:e26403. https://doi.org/10.7554/eLife.26403

Zoppino, F.C.M., R.D. Militello, I. Slavin, C. Alvarez, and M.I. Colombo. 2010. Autophagosome formation depends on the small GTPase Rab1 and functional ER exit sites. *Traffic*. 11:1246–1261. https://doi.org/10.1111/j.1600-0854.2010.01086.x

Supplemental material

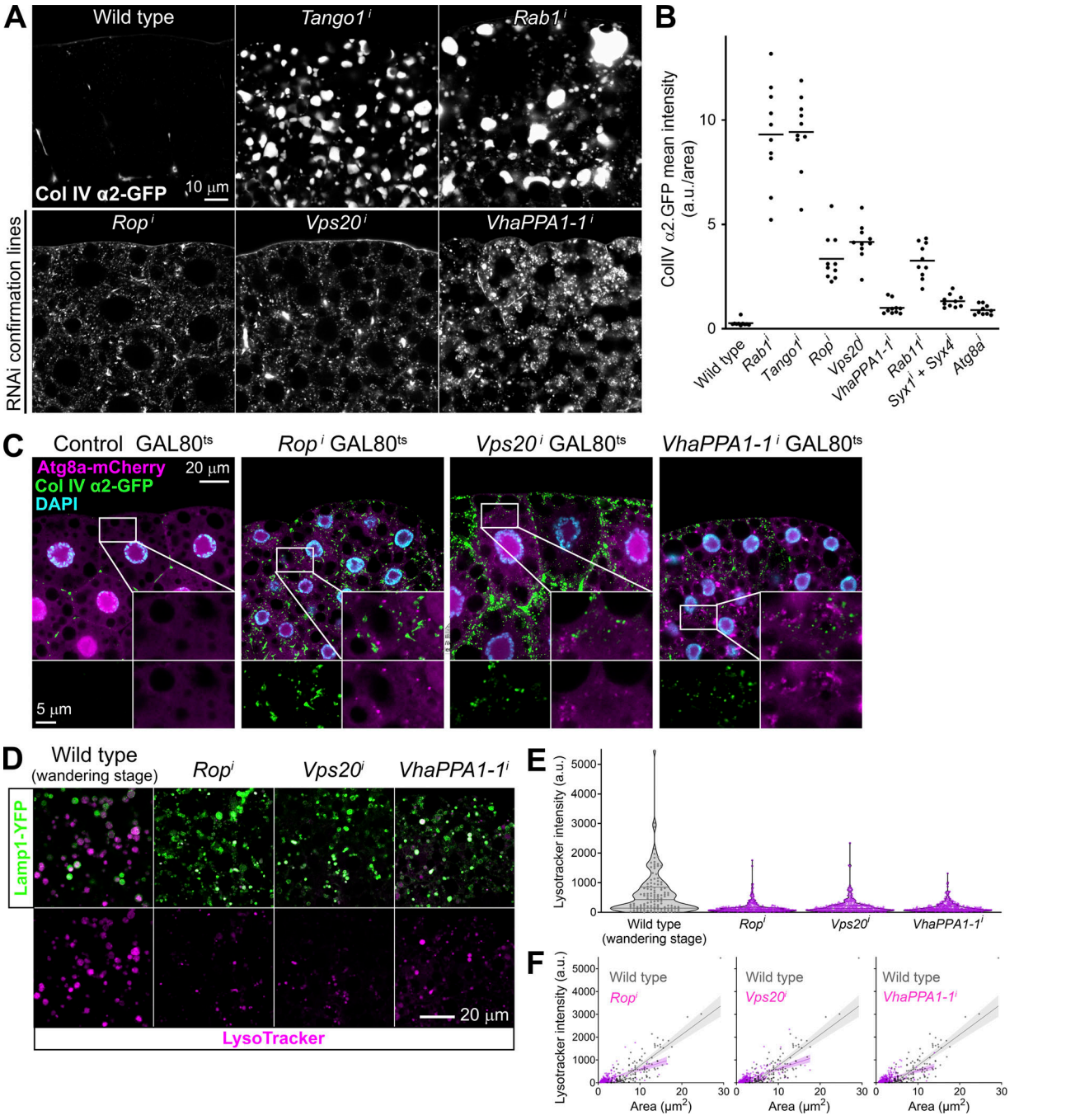

Figure S1. **Confirmation and additional characterization of *Rop*, *Vps20*, and *VhaPPA1-1* hits. (A)** Confocal images of fat body from wild-type, *BM-40-SPARC>Tango1*^{i}, *>Rab1*^{i}, *Rop*^{i} (THU0467), *>Vps20*^{i} (v47653, and *>VhaPPA1-1*^{i} (v47188) L3 larvae showing intracellular accumulation of Collagen IV (α2 chain, Vkg-GFP). Knockdown of Rop, Vps20, or VhaPPA1-1 results in diffuse intracellular accumulation using RNAi transgenic constructs alternative to the ones in the initial screening (Ke et al., 2018). **(B)** Quantification of Collagen IV accumulation in fat body of the indicated genotypes, measured in images like those in A. Each dot represents total Collagen IV–GFP intensity measured in one cell (n = 10 cells per genotype). Horizontal lines mark mean values. Differences with the wild type were significant in unpaired t tests ($P < 0.0001$). **(C)** Confocal images of fat body from *BM-40-SPARC-GAL4+GAL80*^{ts}, *BM-40-SPARC+GAL80*^{ts}*>Rop*^{i} (v19696), *>Vps20*^{i} (THU5269), and *>VhaPPA1-1*^{i} (v47188) L3 larvae (feeding stage) showing localization of Collagen IV (α2 chain Vkg-GFP, green) and *BM-40-SPARC-GAL4*–driven autophagy marker Atg8a-mCherry (magenta). Nuclei in cyan (DAPI). Larvae were dissected 2 d after knockdown initiation (see Materials and methods). Magnified insets in lower right corners show accumulation of Collagen IV distinct from Atg8a puncta in mutant conditions. **(D)** Confocal images of fat body from wild-type L3 larvae (wandering stage), and *BM-40-SPARC>Rop*^{i} (v19696), *>Vps20*^{i} (THU5269), and *>VhaPPA1-1*^{i} (v47188) L3 larvae (feeding stage) showing lysosomal marker Lamp1-YFP (green) and acidification stain LysoTracker Red (magenta, separate channel below). Acidification of autolysosomes is reduced in mutant conditions (compare also TEM images in Figs. 1 E and 9 F). **(E)** LysoTracker intensity measured in images like those in D. The data are presented as violin plots where quartiles are marked, with dots representing individual measurements of vesicle LysoTracker intensity. n = 121, 265, 265, and 100, respectively. **(F)** Plots of LysoTracker intensity vs. vesicle size, measured in images like those in D. Dots represent individual measurements of vesicle LysoTracker intensity (same data as in E) and area in section. Graphs additionally depict linear regression and 99% confidence intervals. The same wild-type data is plotted in all three graphs.

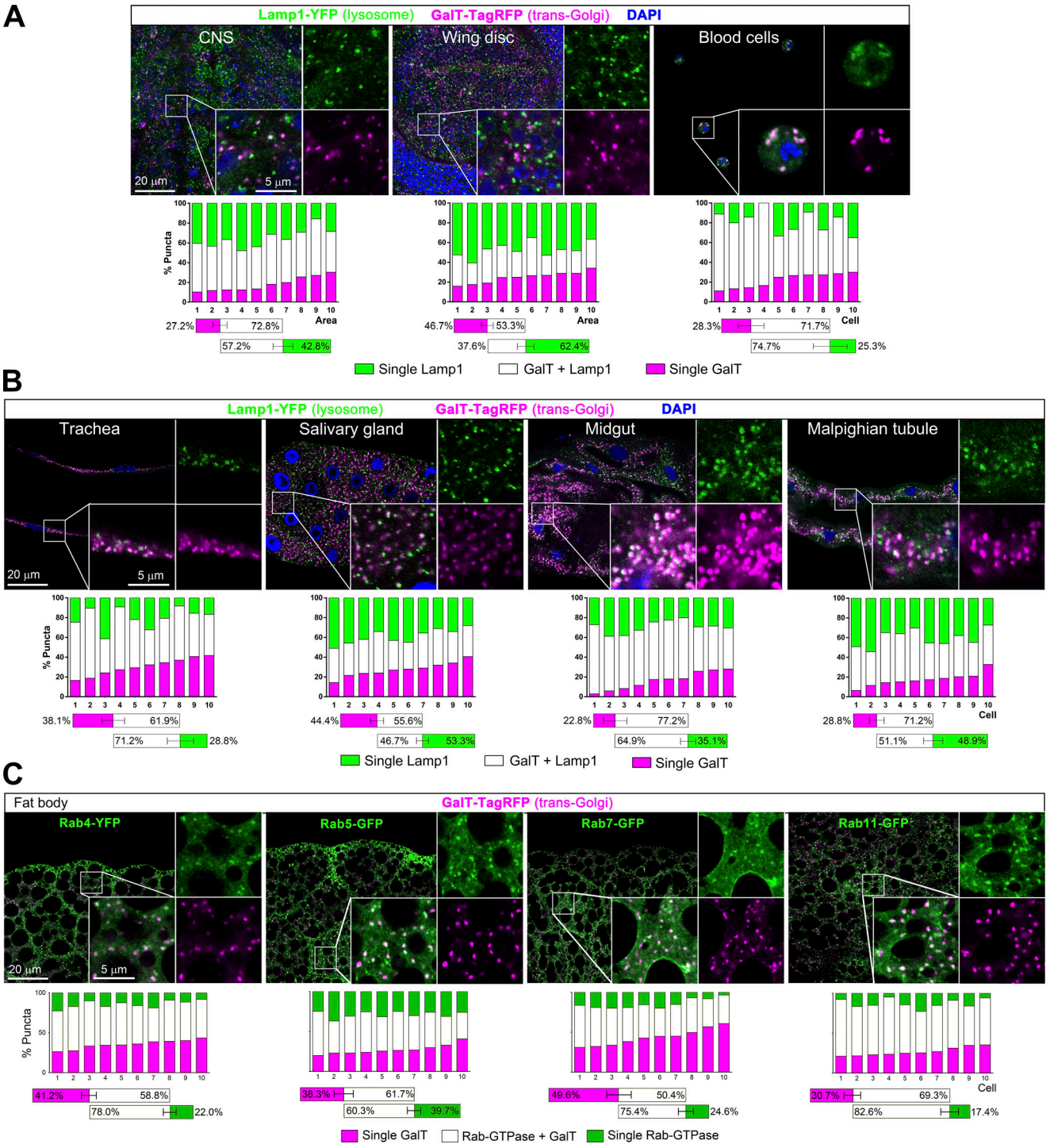

Figure S2. **Lamp1 and endosomal Rab-GTPases associate with the trans-Golgi. (A)** Confocal images showing localization of lysosome marker Lamp1-YFP (green) and trans-Golgi marker GalT-TagRFP (magenta, driven by *act-GAL4*) in L3 CNS, wing imaginal disc, and blood cells. Magnified insets are shown in the lower right corner of each image. Separate channels of magnified insets are shown on the right side. Nuclei stained with DAPI (blue). The graphs below each image quantify lysosome Lamp1 and trans-Golgi GalT puncta proximity measured in 10 different square areas (12.454 × 12.454 µm, CNS and wing disc) or 10 blood cells, as well as average proximity values (n = 10, error bars indicate SD). **(B)** Confocal images showing localization of Lamp1-YFP (green) and GalT-TagRFP (magenta, driven by *act-GAL4*) in L3 dorsal tracheal branch, salivary gland, midgut enteroblasts, and Malpighian tubules. Magnified insets are shown in the lower right corner of each image. Separate channels of magnified insets are shown on the right side. The graphs below each image quantify puncta proximity in 10 different cells, as well as average proximity values (n = 10, error bars indicate SD). **(C)** Confocal images of fat body (feeding stage) showing localization of trans-Golgi marker GalT-TagRFP (magenta) and fluorescently tagged Rab-GTPases Rab4, Rab5, Rab7, and Rab11 (green), all driven by *BM-40-SPARC-GAL4*. Magnified insets are shown in the lower right corner of each image, with separate channels on the right. The graphs below each image quantify Rab-GTPase and trans-Golgi GalT puncta proximity measured in 10 different cells, as well as average proximity values (n = 10, error bars indicate SD). Notice similar percentages of proximity compared to Fig. 2 L.

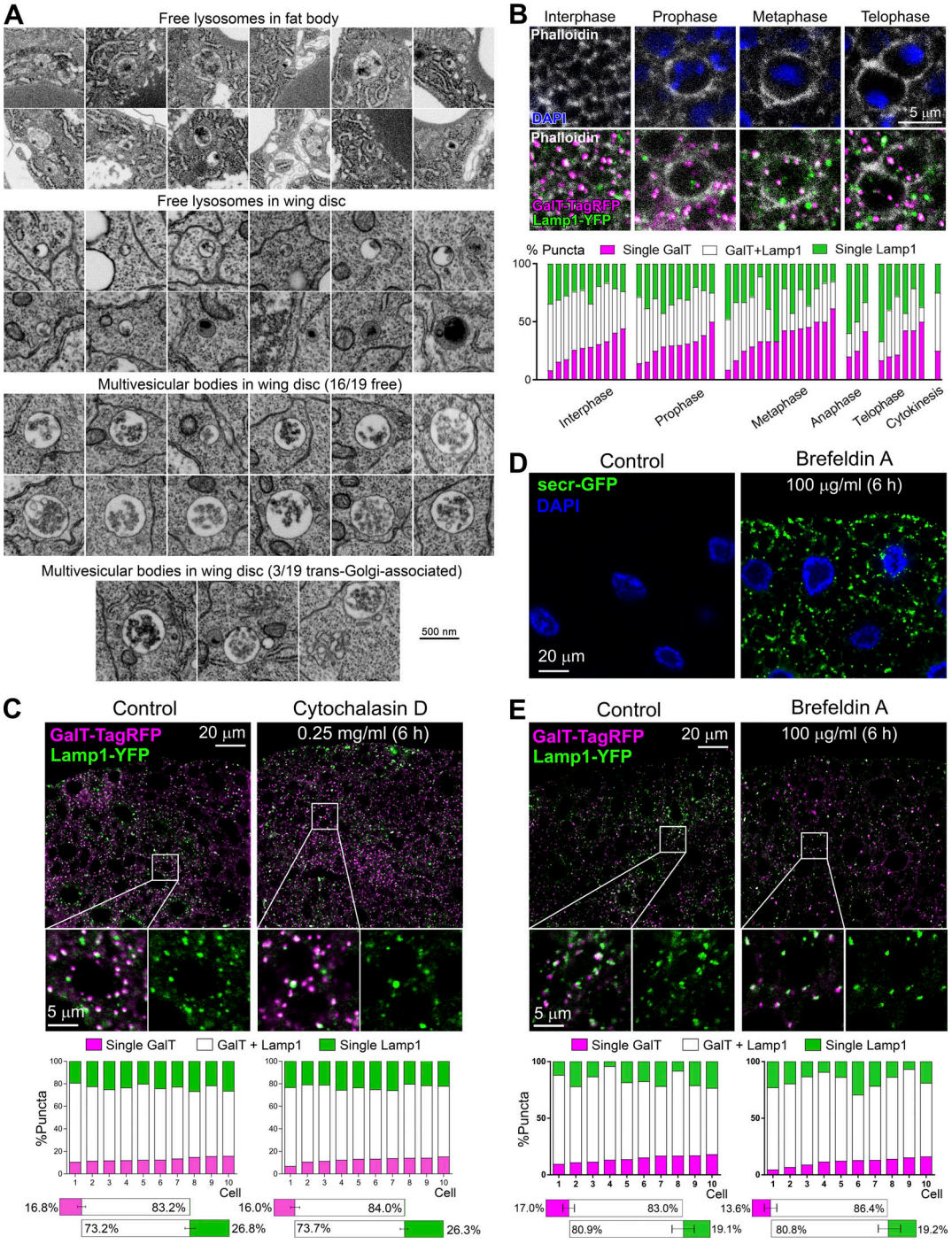

Figure S3. **Additional characterization of free and tGA-lysosomes. (A)** FIB-SEM images showing free lysosomes (not associated to trans-Golgi) in fat body adipocytes and imaginal wing disc epidermal cells, as well as multivesicular bodies in wing disc cells. We did not find similar multivesicular late endosomal structures in fat body of the L3 feeding larva, but their presence has been reported later, upon developmental autophagy induction (Marusz et al., 2015). Multivesicular bodies in wing disc cells are sometimes trans-Golgi–associated (3 out of 19 examples). **(B)** Confocal images of wing disc cells at interphase, prophase, metaphase, and telophase stages of the mitotic cycle. Upper images show F-actin stained with phalloidin (white) and DAPI (blue); lower images show lysosome marker Lamp1-YFP (green) and trans-Golgi marker GalT-TagRFP (magenta, driven by *rn-GAL4*), as well as phalloidin (white). The graphs below quantify Lamp1/GalT puncta proximity measured in individual cells (n = 10, 14, 3, 6, and 1 for prophase, metaphase, anaphase, telophase, and cytokinesis, respectively) or in 6.23 × 6.23 µm areas (interphase, n = 10). **(C)** Confocal images showing Lamp1-YFP (green) and GalT-TagRFP (magenta, driven by *BM-40-SPARC-GAL4*) in L3 fat body (feeding stage) after 6 h culture with (left) or without (right) 0.25 mg/ml of actin polymerization inhibitor Cytochalasin D. Magnified insets are shown below. The graphs quantify puncta proximity in 10 cells, as well as average proximity values (n = 10, error bars indicate SD). **(D)** Confocal images showing distribution of general secretion marker secr-GFP (green, *BM-40-SPARC-GAL4*–driven) in fat body after 6 h culture with (left) or without (right) 100 µg/ml of secretion inhibitor Brefeldin A. DAPI in blue. **(E)** Lamp1-YFP (green) and trans-Golgi marker GalT-TagRFP (magenta, driven by *BM-40-SPARC-GAL4*) in fat body after 6 h culture with (left) or without (right) 100 µg/ml of secretion inhibitor Brefeldin A. Magnified insets are shown below. Graphs quantify puncta proximity as in C.

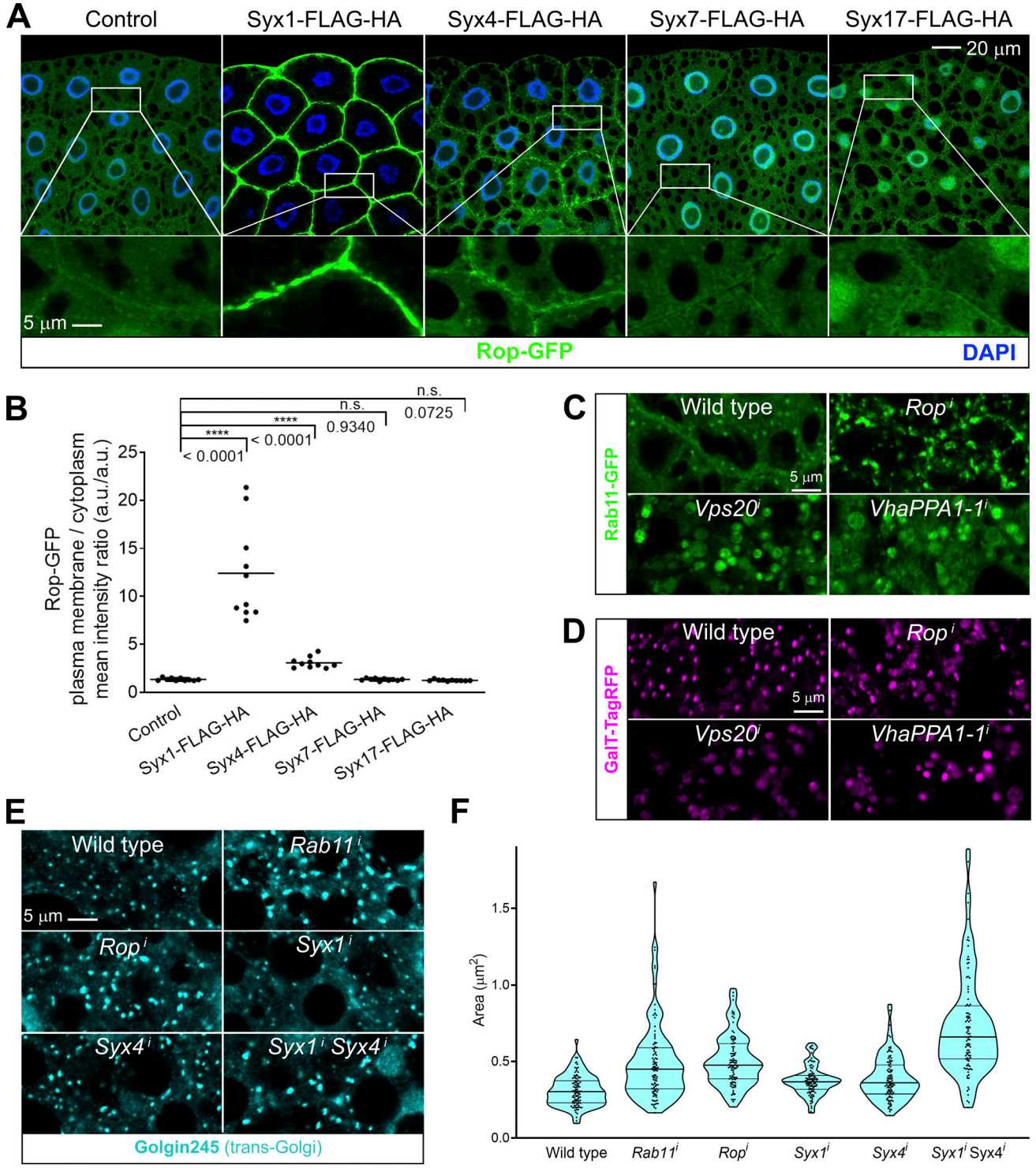

Figure S4. **Syx1 and Syx4 interact with Rop. (A)** Confocal images of fat body expressing Rop-GFP alone (control) or co-expressing Rop-GFP with Syx1-FLAG-HA, Syx4-FLAG-HA, Syx7-FLAG-HA, and Syx17-FLAG-HA, all driven by *BM-40-SPARC-GAL4*. Rectangular insets are shown magnified below. **(B)** Quantification of the recruitment of Rop-GFP to the plasma membrane by Syx1, Syx4, Syx7, and Syx17. Each dot represents the ratio in one cell of Rop-GFP signal intensity between plasma membrane and cytoplasm, measured in images like those in A. n = 10. Horizontal lines mark the mean. P values from unpaired t tests are indicated for differences with the control. n.s., P > 0.05; ****, P < 0.0001. **(C)** Confocal images of fat body from wild-type, *BM-40-SPARC>Rop^i*, *>Vps20^i*, and *>VhaPPA1-1^i* L3 larvae (feeding stage) expressing Rab11-GFP (green). **(D)** Confocal images of fat body from wild-type, *BM-40-SPARC>Rop^i*, *>Vps20^i*, and *>VhaPPA1-1^i* L3 larvae (feeding stage) expressing trans-Golgi marker GalT-TagRFP (magenta). **(E)** Confocal images of fat body from wild-type, *BM-40-SPARC>Rab11^i*, *>Rop^i*, *>Syx1^i*, *>Syx4^i*, and double *>Syx1^i+Syx4^i* L3 larvae (feeding stage) stained with an antibody against trans-Golgi protein Golgin245 (cyan). **(F)** Trans-Golgi size measured in images like those in E. Data are presented as violin plots where quartiles are marked. Dots represent individual punctum size measurements (n = 100 per genotype).

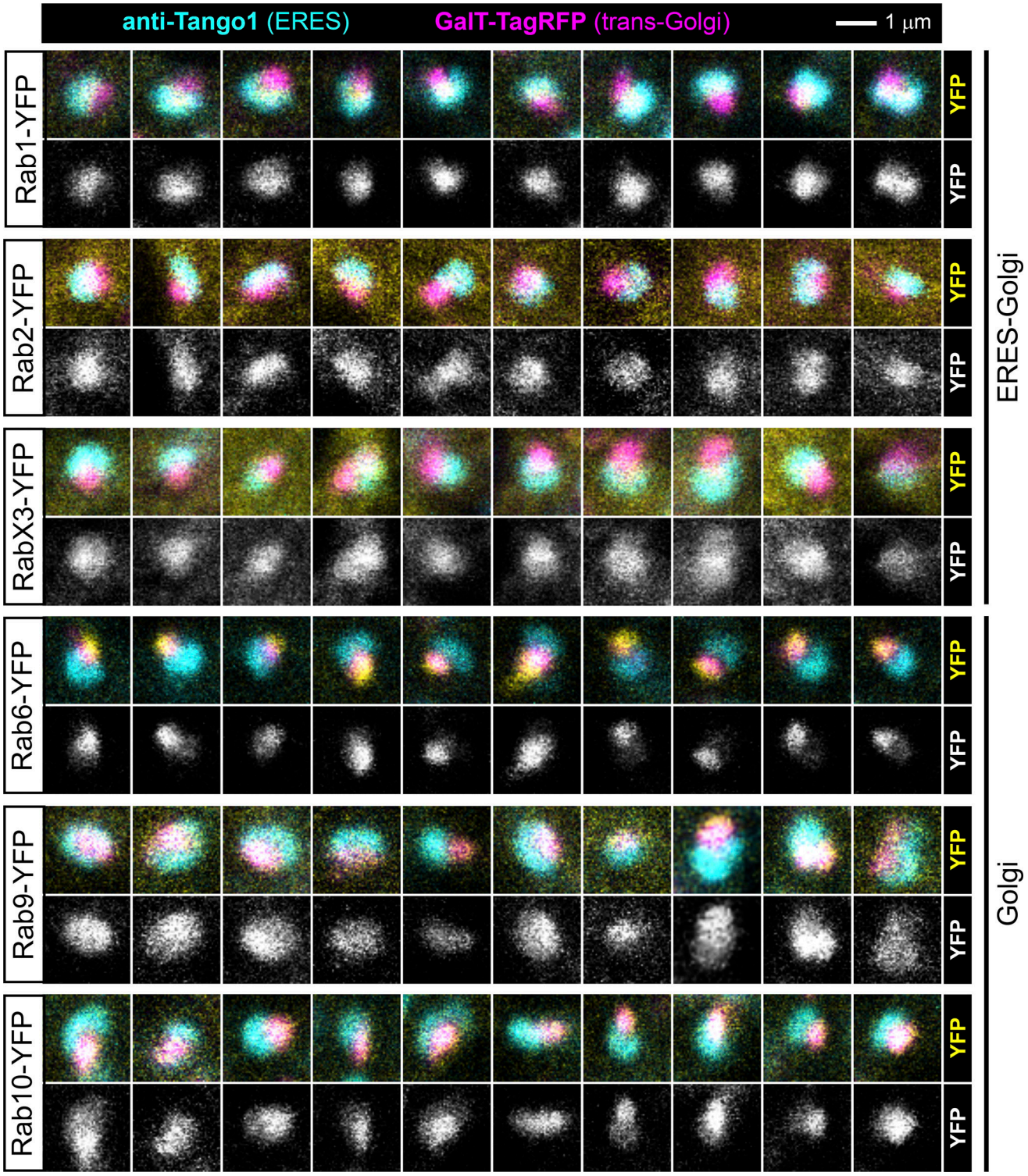

Figure S5. **Localization of Rab1, Rab2, Rab6, Rab9, Rab10, and RabX3 within ERES-Golgi units.** Confocal images of fat body ERES-Golgi units showing localization of the indicated Rab-GTPases (yellow, white in separate channel below) with respect to ERES marker Tango1 (cyan) and trans-Golgi marker GalT (magenta).

Video 1. **FIB-SEM 3D reconstruction of tGA-lysosomes.** Animated 3D renderings of Golgi and tGA-lysosomes reconstructed from FIB-SEM data. ER in green, tGA-lysosomes in yellow, and Golgi in purple. Refer to Fig. 3.

Video 2. **In vivo imaging of trans-Golgi and lysosomes in blood cells.** Time-lapse movie showing examples of lysosome association and dissociation behaviors with respect to the trans-Golgi. Live blood cells expressing lysosomal marker Lamp1-GFP (green) and trans-Golgi marker GalT-TagRFP (magenta), both driven by *BM-40-SPARC-GAL4*, were recorded in a spinning-disc confocal microscope for 10 min each cell at a speed of 10 images/min. Each image is a maximum intensity projection of a 7–9 section stack (*z*-distance 1 µm). Refer to Fig. 4. Time stamp: min:s. Arrowheads point to trans-Golgi associated with dynamic lysosomes. Dashed lines outline cell shape.

Provided online are two tables. Table S1 lists experimental genotypes in the study. Table S2 lists primers used.